Atmos. Meas. Tech. Discuss., 6, 8129–8186, 2013
www.atmos-meas-tech-discuss.net/6/8129/2013/
doi:10.5194/amtd-6-8129-2013


Atmospheric Measurement Techniques Discussions
Open Access



# A rapid method to derive horizontal distributions of trace gases and aerosols near the surface using multi-axis differential optical absorption spectroscopy

**Y. Wang[1], A. Li[1], P. H. Xie[1], T. Wagner[2], H. Chen[1], W. Q. Liu[1], and J. G. Liu[1]**

[1]Anhui Institute of Optics and Fine Mechanics, Chinese Academy of Sciences, Hefei, China
[2]Max Planck Institute for Chemistry, Mainz, Germany

Received: 17 June 2013 – Accepted: 26 August 2013 – Published: 4 September 2013

Correspondence to: T. Wagner (thomas.wagner@mpic.de) and P. H. Xie (phxie@aiofm.ac.cn)

Published by Copernicus Publications on behalf of the European Geosciences Union.







## Abstract

We apply a novel experimental procedure for the rapid measurement of the average volume mixing ratios (VMRs) and horizontal distributions of trace gases such as $NO_2$, $SO_2$, and HCHO in the boundary layer, which was recently suggested by Sinreich et al. (2013). The method is based on two-dimensional scanning multi-axis differential optical absorption spectroscopy (MAX-DOAS). It makes use of two facts (Sinreich et al. 2013): First, the light path for observations at 1° elevation angle traverses mainly air masses located close to the ground (typically < 200 m). Second, the light path length can be calculated using the simultaneous measured absorption of the oxygen dimer $O_4$. Thus, the average value of the trace gas VMR in the atmospheric layer between the surface and the altitude, for which this observation was sensitive, can be calculated. Compared to the originally proposed method, we introduce several important modifications and improvements: We apply the method only to measurements at 1° elevation angles, for which the uncertainties are especially small. Using only 1 elevation angle also allows an increased temporal resolution. We apply correction factors (and their uncertainties) as function of the simultaneously modelled $O_4$ absorption. In this way the correction factors can be directly determined according to the measured $O_4$ dAMF. Finally, the method is extended to trace gases analysed at other wavelengths and also to the retrieval of the aerosol extinction. Depending on the atmospheric visibility, the typical uncertainty of the results ranges from about 15 to 30 %.

We apply the rapid method to observations of a newly developed ground-based multifunctional passive differential optical absorption spectroscopy (GM-DOAS) instrument in the north-west outskirt near Hefei City in China. We report $NO_2$, $SO_2$, and HCHO VMRs and aerosol extinction for four azimuth angles and compare these results with those from simultaneous long-path DOAS observations. Good agreement is found (squares of the correlation coefficients for $NO_2$, $SO_2$, and HCHO were 0.92, 0.84, and 0.59, respectively), verifying the reliability of this novel method. Similar agreement is found for the comparison of the aerosol extinction with results from visibility meters.





AMTD
6, 8129–8186, 2013



Future studies may conduct measurements using a larger number of azimuth angles to increase the spatial resolution.

## 1 Introduction

Nitrogen dioxide ($NO_2$), sulfur dioxide ($SO_2$), and formaldehyde (HCHO) are important atmospheric constituents which play crucial roles in tropospheric chemistry (Crutzen, 1979; Lurmann et al., 1992; Ho et al., 2002; Hellén et al., 2004; Smith et al., 2011). $NO_2$ partly controls the lower atmospheric oxidizing capacity. HCHO is important for estimating photochemical processes. Sulfate aerosols formed by $SO_2$ are sources of inhalable particles. Nowadays, anthropogenic emissions from traffic, industry, and biomass burning have significantly increased the concentrations of these gases in the boundary layer directly affecting air quality and human health (Environmental Protection Agency, 1998; Seinfeld and Pandis, 1998). To understand the influences of these gases to the atmospheric chemistry processes and to formulate effective strategies for pollution regulation, studying the spatial and temporal distribution of these gases is necessary.

The horizontal distribution of trace gases in the boundary layer is usually inhomogeneous near strong emission sources. Investigating the horizontal distribution of trace gases is useful for atmospheric chemistry research and environment pollution treatment. Passive differential optical absorption spectroscopy (DOAS) (Platt and Stutz, 2008) is a widely used technique to measure the distribution and variation of trace gases such as $NO_2$, $SO_2$, and HCHO. Satellite DOAS has been widely used to study the global distribution of trace gases (Bovensmann et al., 1999; Burrows et al., 1999; Wagner et al., 2008). However, this technique focuses on the large-scale horizontal distribution. Mobile DOAS is useful for studying the horizontal distribution (Johansson et al., 2008, 2009; Wagner et al., 2010; Wu et al., 2013) but requires comparatively large efforts. Tomographic target light scattering (TOTAL) DOAS (Frins et al., 2006, 2008; Wang et al. 2012) is a novel method for studying high spatial resolution surface-near





AMTD
6, 8129–8186, 2013



distributions of trace gases. However, the application of TOTAL DOAS relies on the availability of well-suited targets. Furthermore, the viewing directions cannot be freely chosen.

Multi-Axis- (MAX-) DOAS is an inexpensive tool for measuring the tropospheric vertical distribution of trace gases (Hönninger et al., 2004; Bobrowski et al., 2003; Wittrock et al., 2004; Heckel et al., 2005; Pikelnaya et al., 2007; Sinreich et al., 2007; Theys et al., 2007; Clemer et al., 2009; Vlemmix et al., 2010, 2011; Frieß et al., 2011; Irie et al., 2011; Wagner et al., 2011; Li et al., 2012; Yilmaz, 2012). Concentration profiles of trace gases in the boundary layer can be derived from MAX-DOAS observations using different inversion techniques, e.g. the optimal estimate method (Frieß et al., 2011; Yilmaz, 2012) or a look-up table approach (Li et al., 2010, 2012; Wagner et al., 2011). These methods usually apply a two step procedure and are rather time consuming.

A novel retrieval technique based on ground-based MAX-DOAS observations was recently proposed by Sinreich et al. (2013): The effective light path length in the boundary layer determined by $O_4$ dSCD for low elevation angles is used to convert the dSCD of trace gases into surface-near mixing ratios. Compared to a full profile inversion from MAX-DOAS observations, this method is much simpler and faster, but can also be subject to larger uncertainties in specific situations (see below). In our study we use this new retrieval technique, but apply several important modifications:

a. We only use measurements at 1° elevation angle. For such low elevation angles the influence of the relative profile shape of the trace gases or aerosols on the retrieved results is smaller than for higher elevation angles (and in most cases the correction factors are closer to unity). The restriction to only one elevation angle (besides zenith view) also leads to a higher temporal and spatial resolution.

b. We parameterize the calculated correction factors (and their uncertainties) as function of the simultaneously modeled differential air mass factors (dAMF) of $O_4$ (Martin et al., 2002; Eskes and Boursma, 2003; Frins et al., 2006; Richter and Wagner, 2011). Using this parameterisation, appropriate correction factors for a





AMTD
6, 8129–8186, 2013



given measurement can be directly determined according to the measured $O_4$ dAMF.

c. We develop a method to extrapolate the effective light path lengths from the wavelength of the $O_4$ measurement (here 360 nm) to other wavelengths. This allows the extension of the method to trace gases which are retrieved at wavelengths different from those of the $O_4$ absorptions (like e.g. $SO_2$).

d. In addition to the trace gas VMRs close to the surface we also retrieve the surface-near aerosol extinction.

We apply the rapid method to a newly developed two-dimensional (2-D) MAX-DOAS instrument, which can point to any azimuth and elevation angle. Using the new technique, information on the horizontal distribution of surface-near trace gas VMR close to the experimental site with a time resolution of approximately 2 min can be obtained. Aside from circularly measuring spectra at 1° elevation angle, also observations at 90° are made to obtain the differential slant column density (dSCD) of the trace gases. Given that the light path for observations at 1° elevation angle is located near the ground (typically $< 200$ m) and its length can be calculated using the simultaneous measured absorption of the stable oxygen dimer $O_4$, the average volume mixing ratios (VMR) of the trace gases near the ground can be calculated.

In this paper, we first discuss the details of the method using the full-spherical radiative transfer model (RTM) SCIATRAN 2.2 (Rozanov, 2005). Then, we present results of rapid $NO_2$, $SO_2$, and HCHO VMR measurements for four azimuths in the north-west outskirt near Hefei City in China using GM-DOAS. The accuracy of the rapid MAX-DOAS method is discussed in comparison with long-path (LP) DOAS (Qin et al., 2006). Furthermore, the horizontal distribution and main sources of trace gases and aerosols are analyzed based on the divergences of the results for the four azimuth angles (AAs). Finally, the error sources of the average VMR of trace gases in this rapid MAX-DOAS method are discussed.





AMTD
6, 8129–8186, 2013



## 2 Retrieving the average VMR of trace gases close to the surface from low elevation MAX-DOAS observations

The direct light path along the line of sight for observations at a low elevation angle is located close to the surface. Thus such observations are mostly sensitive to surface-near trace gases. The effective length of the direct light path is determined by the atmospheric visibility and thus by scattering on air molecules and aerosol particles. Since the concentration of air molecules is almost constant, the effective length of the direct path is determined by the concentration and optical properties of atmospheric aerosols. In contrast, above the altitude, from which most of the solar photons are scattered into the line of sight of the instrument, the atmospheric light path is mainly determined by the position of the sun. Thus, except for measurements at very high solar zenith angles (SZA), the light path crosses these altitudes at rather large angles (with respect to the horizon) and thus the sensitivity of the measurement to these altitudes is much lower compared to the near surface layer. The weighting of the measurement sensitivity towards the surface is further enhanced by the fact that for the spectral analysis of our MAX-DOAS observations a so called Fraunhofer reference spectrum is used to remove the strong Fraunhofer lines in the measured spectrum. Thus the dSCD derived from the DOAS analysis (see Sect. 4.1) represents the difference of the slant column densities of both measurements. Since the Fraunhofer reference spectrum is measured in zenith direction, the derived dSCD mostly represents the trace gas concentration integrated along the direct light path, while the absorptions from the atmosphere above mainly cancel.

These basic dependencies are discussed in detail in the recently published study of Sinreich et al. (2013). They also developed a parameterized algorithm to convert the measured dSCDs of $O_4$, $NO_2$ and HCHO at low elevation angles to box-averaged mixing ratios of $NO_2$ and HCHO.





AMTD
6, 8129–8186, 2013



As suggested by Sinreich et al. (2013), the effective light path length ($L$) can be calculated from the retrieved $O_4$ dSCD:

$$L = \mathrm{dSCD}_{O_4} / c_{O_4}. \quad (1)$$

The $O_4$ concentration is proportional to the square of the $O_2$ concentration (Greenblatt et al., 1990; Wagner et al., 2002) and thus varies only slightly with time (due to variations of temperature and pressure). Note that since the $O_4$ concentration itself is not known, the $O_4$ absorption is usually related to the square of the $O_2$ concentration (Greenblatt et al., 1990). Accordingly, the $O_4$ dSCD is expressed in units of molecules$^2$ cm$^{-5}$. The surface-near $O_4$ concentration ($c_{O_4}$) can been calculated as $2.79 \times 10^{37}$ molecules$^2$ cm$^{-6}$ using local atmospheric temperature and pressure. Here it should be noted that $L$ is not the absolute light path length for the observation at 1° elevation angle, but the difference between the light path lengths for the observation at 1° elevation angle and the Fraunhofer reference spectrum made in zenith direction. Note that the effective light path length derived in Eq. (1) is representative for 360 nm because it was derived from the $O_4$ absorption band at 360 nm. It can be transformed for other wavelength ranges of 340 and 310 nm in Eqs. (7) and (8) (see Sect. 2.1).

Using this effective light path length derived in Eq. (1) (for the wavelength dependence of $L$ see below) , the average trace gas concentration (and from that also the VMR) near the ground can be calculated from the derived trace gas dSCD:

$$c = \mathrm{dSCD} / L. \quad (2)$$

It was shown by Sinreich et al. (2013) that using this simple retrieval scheme, systematic errors are introduced, if the relative profile of the considered trace gas differs from that of $O_4$. For atmospheric pollutants, this is generally the case: Since they are emitted mainly from sources close to the surface, their abundances are typically largest at low altitudes, but decrease rapidly with altitude, especially above the boundary layer. Sinreich et al. (2013) suggested to apply correction factors to the results derived from Eq. (2):





AMTD
6, 8129–8186, 2013



$$c_{\mathrm{corr}} = c / f_{\mathrm{corr}}. \quad (3)$$

These correction factors are derived from radiative transfer simulations assuming different profiles of trace gases and aerosols (for details see Sinreich et al., 2013, and Sect. 2.2). Here it is important to note that in contrast to higher elevation angles the correction factors for an elevation angle of 1° are usually closer to unity than for higher elevation angles. This indicates that the very low elevation angles are particularly well suited for the application of the simple parameterized retrieval technique. Also the uncertainties of the correction factors for 1° elevation are typically small: depending on the atmospheric visibility and the considered trace gas it is usually between 15 and 30 % (see Sect. 2.2).

### 2.1 Extrapolation of the effective light path length to other wavelengths

Considering the wavelength dependence of Rayleigh and aerosol scattering, the effective light path $L$ should systematically vary with wavelength. Since the light path length based on the $O_4$ information is obtained at 360 nm, it is not exactly representative for other wavelengths. Therefore, extrapolating $L$ to other wavelength ranges for retrieving trace gases such as $SO_2$ (310 nm) and HCHO (340 nm) based on the derived length of the light path from $O_4$ information at 360 nm is an important aspect. The relationships between the light path lengths at 310 and 340 nm to those at 360 nm were studied using SCIATRAN for a variety of aerosol scenarios. The aerosol types of the aerosol scenarios were classified as "urban" (single scattering albedo of 0.925 and asymmetry factor of 0.703 at 550 nm) in the boundary layer and "continental average" (single scattering albedo of 0.817 and asymmetry factor of 0.689 at 550 nm) in the free troposphere layer based on the software package OPAC (Hess et al., 1998). We assumed that the aerosol profiles contain two layers, namely, the atmospheric boundary layer and the free troposphere layer. The layers can be described using three parameters, namely, aerosol optical depth ($\tau$), fraction ($F$) of $\tau$ in the boundary layer, and height ($H$)





AMTD
6, 8129–8186, 2013



of the boundary layer (Li et al., 2010). The aerosol extinction profile $E(z)$ in the range of 0 to 15 km was assumed as follows:

$$E(z) = \begin{cases} \tau \cdot F/H & z \le H \\ \beta \cdot \exp(-z/\xi) & z > H \end{cases}. \quad (4)$$

Here $\beta$ is the normalizing constant for the exponential factor and can be calculated using Eq. (5)

$$\beta = \frac{(1 - F) \times \tau}{\xi \times \left(e^{-H/\xi} - e^{-15\text{km}/\xi}\right)}. \quad (5)$$

Here $\xi$ is the scaling height for the aerosol in the free tropospheric layer, which was set as 5 km. The three parameters for 60 aerosol scenarios generated are shown in Table 1.

$O_4$ dAMF were calculated for three wavelengths (310, 340, 360 nm) using RTM based on the assumed aerosol scenarios and were transformed into the respective $O_4$ dSCDs using a value for the $O_4$ VCD of $1.19 \times 10^{43}$ molecules$^2$ cm$^{-5}$ in Eq. (6). The $O_4$ VCD was calculated using the standard pressure and temperature profiles in May at the northern latitude of 35° from the climatological database developed by MPIC Mainz (Brühl and Crutzen, 1993).

$$\text{dSCD}_{O_4} = \text{dAMF}_{O_4} \times \text{VCD}_{O_4} \quad (6)$$

Then, the corresponding effective light path lengths were calculated from the $O_4$ dSCDs using Eq. (1). The surface elevation of the measurement site (approximately 50 m a.s.l. – above sea level) was considered. We performed simulations for three SZAs (20, 40, and 50°) and relative azimuth angles (RAAs) (30, 90, and 180°).

The light path lengths at 310 nm as a function of the light path lengths at 360 nm are plotted in Fig. 1. A second-order polynomial was fitted to the simulation results with a square correlation coefficient of approximately 1. The statistical parameters of this





AMTD
6, 8129–8186, 2013



curve are also shown in Fig. 1. From the close relationship we conclude that the light path length at 310 nm ($L_{310}$) can be obtained based on the light path length at 360 nm ($L_{360}$) using the fitted polynomial:

$$L_{310} = 0.136 + 0.897 \times L_{360} - 0.023 \times L_{360}^2. \quad (7)$$

For HCHO, the fit curve and parameters of the light path lengths (represented as dots) at 340 nm ($L_{340}$) against $L_{360}$ are shown in Fig. 2. Again, $L_{340}$ can be calculated from $L_{360}$ using the fitted polynomial:

$$L_{340} = -0.017 + 1.003 \times L_{360} - 0.011 \times L_{360}^2. \quad (8)$$

Since the effective light path lengths depend on the aerosol load, also the altitude ranges, for which the trace gas VMR is derived by Eq. (2), depends on the aerosol load. This so called sensitive altitude range ($h$) can be briefly calculated from $L$ using the geometric approximation (Sinreich et al., 2013):

$$h = L \times \sin(1^\circ). \quad (9)$$

With $\sin(1^\circ) = 0.0175$, for typical values of $L$ ($L < 10$ km as shown in Fig. 13), the layer height $h$ is below 200 m.

## 2.2 Calculation of correction factors

Because of the different vertical profile shapes of $O_4$ and the atmospheric pollutants ($NO_2$, HCHO, $SO_2$), the VMRs calculated using Eqs. (1) and (2) are usually different from the true surface-near VMRs. To correct these deviations, correction factors (Eq. 3) were suggested by Sinreich et al. (2013). The correction factors are derived from RTM using assumptions on the profile shapes of the trace gases and aerosols:

$$f_{corr} = \frac{c_{retrieved}}{c_{real}} = \frac{dSCD_{tracegas}}{L \cdot c_{real}}. \quad (10)$$





AMTD
6, 8129–8186, 2013



$c_{real}$ is the real surface-near trace gases concentration which was used as input in the RTM. $c_{retrieved}$ is derived from the simulated trace gas dSCD. $L$ is calculated from the simulated $O_4$ dSCD using Eq. (1). Note that the correction factors for 310 and 340 nm were calculated using the modified values of $L$ based on Eqs. (7) and (8). We calculate correction factors for an elevation angle of 1° at the wavelengths used in this study (310, 340, 360 nm).

For the trace gases we assumed homogenous box layers with altitudes of 0.5, 1 and 2 km (see Sinreich et al., 2013). For the aerosols, we used the profiles introduced in Sect. 2.1 (see Table 1). Figure 3 shows the dependence of the correction factors for a fixed trace gas profile (1 km box profile) on the different aerosol scenarios. The calculations are performed for 360 nm and for a RAA of 90° and SZA of 20°. The correction factors are plotted as function of the $O_4$ dAMF which is also derived from the RTM. The parameterisation of the correction factors as function of the $O_4$ dAMF is very important, because appropriate correction factors for a given measurement can thus be directly determined according to the measured $O_4$ dAMF.

The results shown in Fig. 3a indicate that the uncertainty of the correction factors caused by variations of the aerosol profile systematically increases with increasing AOD (decreasing atmospheric visibility). The results in Fig. 3b indicate that the variation of aerosol layer heights causes the strongest variation of the correction factors.

Also the variation of the trace gas profiles has an influence on the correction factors. Like in Sinreich et al. (2013) we assumed box profiles of 0.5, 1 and 2 km for the trace gases. Although for individual observations the true trace gas profiles might be substantially different from such box profiles, the selected trace gas profiles are probably largely representative for the profiles of atmospheric pollutants.

Figure 4 shows the correction factors for the different trace gas box heights including the variations caused by the different aerosol profiles (as shown in Fig. 3). The results indicate that the trace gas profile typically has the strongest influence on the correction factors. Because both the profiles of the trace gases and aerosols are usually unknown for actual measurements, we calculate mean values of the correction factors





AMTD
6, 8129–8186, 2013



for all combinations of trace gas and aerosol profiles as function of the $O_4$ dAMF (second order polynomial, green line in Fig. 4). This polynomial can be used as correction factor based on the measured $O_4$ dAMF. In addition, also the maximum and minimum values of the correction factors as function of the $O_4$ dAMF are determined (using a polynomial fit to the minimum or maximum values in selected $O_4$ dAMF bins). From these fitted polynomials (magenta and yellow lines in Fig. 4), the uncertainty of the average correction factors can be quantified.

In addition to the dependence on the trace gas and aerosol profiles, the correction factors also systematically depend on the viewing geometry (RAA and SZA). As shown in Fig. 5, these dependencies can become rather large. However, in contrast to the trace gas and aerosol profiles, the viewing geometry for a given measurement is exactly known and can be taken into account in the calculation of the correction factors.

In this study correction factors are calculated following two different strategies:

a. Average, minimum and maximum correction factors (as function of the $O_4$ dAMF, see Fig. 4) are calculated for a large number of combinations of SZA and RAA. These results constitute a universal data base, which can be used to correct any (future) measurements using our parameterized technique. The coefficients of the fitted polynomials (average, minimum and maximum correction factors as function of the $O_4$ dAMF) for all combinations of RAAs of 0, 45, 90, 135 and 180° and SZAs of 20, 30, 40, 50, 60, 70 and 80° will be given in the Supplement.

b. In order to provide correction factors for the measurements in this study, correction factors as function of the $O_4$ dAMF are calculated for the each specific combination of SZA and RAA based on the exact time of each measurement. These correction factors (and the respective maxima and minima) according to the measured $O_4$ dAMF of the selected measurement are used to calculate the trace gas VMRs and the associated uncertainties (Eq. 3).

Since HCHO and $SO_2$ are analysed in different wavelength ranges, appropriate correction factors for these wavelengths have to be calculated. In Fig. 6 the relationships





AMTD
6, 8129–8186, 2013



between the correction factors for 310 nm ($SO_2$) and 340 nm (HCHO) and those for 360 nm ($NO_2$) are shown. We find that the HCHO correction factors are very similar to those for $NO_2$, thus the $NO_2$ correction factors can also be used to correct the HCHO VMRs. In contrast, the correction factors for $SO_2$ are rather different from those for $NO_2$, particularly for $NO_2$ correction factors between 0.8 and 1.1 (Fig. 6). So $SO_2$ correction factors should be calculated and applied separately.

## 3 Instrument and experiment strategy

### 3.1 The GM-DOAS instrument

A new GM-DOAS instrument, which has many optional operating patterns, was developed by our group (Fig. 7). The instrument includes a quartz telescope (field of view angle of 0.2°) with ultraviolet-anti-reflection. The telescope is carried by a 2-D motor, which is located outdoors on an elevated platform to collect scattered sunlight. The 2-D motor can point the telescope to any direction with a precision of 0.05° based on the feedback of the electronic inclinometer with a precision of 0.01°. The light is focused onto a 10 m fiber bundle consisting of 7 × 200 µm silica fibers. The end of the fiber bundle is directed onto the entrance slit (with 200 µm width) of the spectrometer. The spectrometer (Princeton Instrument Acton SP500i Imaging Czerny-Turner spectrometer) has 600 grooves $mm^{-1}$ grating (300 nm blaze angle and 83 nm range) and a charge-coupled device (CCD) camera (back-illuminated 2-D CCD detector, 2048 × 512 pixels). The spectrometer is cooled to −50 °C to reduce dark current. The computer is placed indoors in an air-conditioned lab. The data of the imaging channels are binned to reduce random noise. A background spectrum is obtained by closing the shutter in front of the slit. This background spectrum uses the same integration time and number of scans as the latest measured spectrum. Thus, the background spectrum includes the offset and dark current of the detector. The background spectrum is subtracted





AMTD
6, 8129–8186, 2013



from the measured spectrum allowing the correction of dark and offset current. The spectral resolution of the instrument (full width at half maximum) is 0.35 nm.

The experiment site is approximately 6 km away from the urban center and located in the north-west outskirts of Hefei City (Fig. 8). The telescope was circularly pointed to four AAs (0, 90, 130, and 170°). These angles correspond to the following areas: farming region, industrial area, downtown, and economic development zone. The experiment was performed from 08:00 to 16:00 LT (local time) on mostly sunny days (16, 18, and 21 May as well as 3 June 2012); the corresponding SZAs are always $< 60°$.

### 3.2 The LP-DOAS instrument

A LP-DOAS instrument was operated near the GM-DOAS instrument at a distance of less than 100 m. From the LP-DOAS observations trace gas VMR of $NO_2$, HCHO, and $SO_2$ are determined, which are well suited for comparison with the GM-DOAS observations. The LP-DOAS instrument consists of an artificial light source (xenon arc lamp) and a coaxial Newtonian telescope with combined transmitting and receiving optic fibers. A retro reflector array (located 350 m away and approximately 30 m above the ground) is used for reflecting the light exactly back into the telescope, where it is focused onto a quartz fiber. The quartz fiber transmits the light into a spectrograph. Given that the total light path is approximately 700 m, the integrated column density along the light path can be easily and exactly transformed into VMR.

## 4 Data analysis, comparison with LP-DOAS, and discussion

### 4.1 Spectral retrieval of $O_4$, $NO_2$, $SO_2$, and HCHO

Based on the Lambert-Beer law, different trace gases can be retrieved using the DOAS algorithm in different spectral ranges. We used the WINDOAS software (Fayt and van Roozendael, 2009) to analyze the measured spectra. The fitted polynomial degree was three. The effect of Raman scattering was compensated by fitting a synthetic Ring





AMTD
6, 8129–8186, 2013



spectrum (Grainger and Ring, 1962; Solomon et al., 1987; Wagner et al., 2009) as an additional absorber. This Ring spectrum was computed using the DOASIS software (Kraus, 2006). The absorption cross sections of $O_4$ at 296 K (Greenblatt et al., 1990), $NO_2$ at 294 K (Vandaele et al., 1998), HCHO at 298 K (Meller et al., 2000), $O_3$ at 223 K (Bogumil, 2003) and $SO_2$ at 293 K (Bogumil, 2003) are used in the DOAS fits.

For $NO_2$ and $O_4$, the spectra were analyzed in the wavelength range of 336 to 370 nm. The window contains two absorption bands at 343 and 360 nm. Here, it should be noted that the derived $O_4$ dSCD is dominated by the much stronger $O_4$ absorption at 360 nm. Besides the cross sections of $O_4$ and $NO_2$, also the cross sections of $O_3$ and HCHO were considered. An example of the spectral fit from 5 May 2012 at 12:45 LT is shown in Fig. 9.

Figures 10 and 11 show typical examples of HCHO and $SO_2$ fits in the spectral ranges of 322 to 356 nm, and 308 to 325 nm, respectively. The determined trace gas dSCDs for the selected examples are as follows: the $NO_2$ dSCD was $1.2 \times 10^{16}$ molecules cm$^{-2}$ the HCHO dSCD was $2.94 \times 10^{16}$ molecules cm$^{-2}$, and the $SO_2$ dSCD was $2.16 \times 10^{16}$ molecules cm$^{-2}$. The effective light path lengths derived from the $O_4$ dSCD (and according to Eqs. (7) and (8) are 7.8, 7.1, and 5.7 km for 360, 340, and 310 nm, respectively. Using these results, the following trace gas VMR were derived: for $NO_2$: 0.6 ppb, for HCHO: 1.7 ppb, and for $SO_2$: 1.5 ppb.

The DOAS fit examples for LP-DOAS are shown in Fig. 12. All absorption cross sections for LP-DOAS are the same as for the rapid MAX-DOAS method (GM-DOAS). For $NO_2$ the same fitting window as for the GM-DOAS was selected. For $SO_2$ and HCHO, a different fitting window (from 290 to 320 nm) was used, which is more suitable according to the specific properties of the LP-DOAS instrument.

### 4.2 Differential light path lengths and correction factors

The differential light path lengths near the ground at 360 nm were calculated based on the $O_4$ information for four days using Eq. (1) (Fig. 13). Figure 14 shows the corresponding sensitive altitude ranges that were geometrically calculated using Eq. (9). The





AMTD
6, 8129–8186, 2013



diurnal variation of the light path lengths (usually smaller $L$ in the morning and evening) is probably a consequence of the varying aerosol extinction close to the surface. The results indicate that the horizontal distance, for which MAX-DOAS observations at 1° elevation angle are sensitive for, can reach approximately 6 to 9 km at noon, which corresponds to sensitivity altitude ranges up to approximately 100 and 160 m. Slightly lower effective light path lengths and sensitivity altitude ranges were derived for 340 and 310 nm using Eqs. (7)–(9) (not shown). Interestingly, the results for the different AAs are very similar and show the same diurnal variations. However, the effective light path lengths at the north view are typically slightly larger than those of the other directions. This result indicates smaller aerosol extinction at the north view.

To show the effects of the aerosol load on the light path lengths, the AOD at the experimental site was obtained from the daily data of MODIS Level 3 Atmosphere Products (MOD 08_D3, National Aeronautics and Space Administration, 2012) shown in Fig. 15. In addition, the average light path lengths of the four days for the time of the MODIS overpass (±30 min) are shown. It should be noted that no direct (anti-) correlation of the AOD and the effective light path length can be expected because the aerosol extinction close to the surface accounts only for a part of the total AOD. Nevertheless, it is found that the lower AOD (on 18 and 21 May) corresponds to longer effective light path lengths on those days.

The time series of the average correction factors and their corresponding uncertainties of $NO_2$, HCHO and $SO_2$ for four azimuth angles during the period of the experiment are determined based on measured $O_4$ dAMF. Especially in the morning (and for high aerosol load), the uncertainties of the correction factors for the viewing direction with azimuth angle of 90° can become rather large. This is caused by the small RAA for these measurements. In order to keep the uncertainty of the retrieved trace gas VMRs low, the results for azimuth angle of 90° before 10:00 LT are deleted on 16, 18, and 21 May.





AMTD
6, 8129–8186, 2013



### 4.3 Results and comparisons

Before we report and discuss the average $NO_2$, $SO_2$, and HCHO VMRs in the boundary layer derived from four azimuth angles using the rapid MAX-DOAS method, we give a brief overview on some meteorological parameters on the four selected days. Wind directions and speeds are shown in Fig. 16. The main wind direction during the four days was south-east except on 16 May when the main wind direction was south-west (Fig. 16a). The time series of the hourly average wind speed (Fig. 16b) indicates that the air mass transport was more effective during daytime.

Figures 18–20 show the time series of average $NO_2$, $SO_2$, and HCHO VMRs for 0, 90, 130, and 170° azimuths, respectively, as well as the corresponding VMR derived from LP-DOAS for comparison. Figure 21a–c present the daily mean values of the three trace gases for the different directions. For the four azimuths, similar daily evolutions of the trace gas VMR are found confirming that no strong horizontal inhomogeneities were present in the surrounding area (according to an effective light path length of 6 km, this area is approximately 130 $km^2$). Interestingly, on 21 May, larger differences are found indicating significant gradients of the trace gas VMR around the measurement site. Stronger gradients on that day are also indicated by the rapid temporal variations of the VMR of $NO_2$ and $SO_2$ retrieved from LP-DOAS. Here it should be noted that the LP-DOAS monitors the average VMR over a rather short distance of 350 m. By contrast, the rapid MAX-DOAS method measures large-scale (2 to 9 km) average VMRs. Therefore, the temporal variations of the rapid MAX-DOAS method are much smoother than those of the LP-DOAS measurements.

To verify the reliability of the rapid MAX-DOAS method, linear regression curves and statistical parameters of the average hourly VMR from LP-DOAS and MAX-DOAS for the three trace gases were calculated (Fig. 21). The AAs of the measurement were not distinguished in the statistical process. The squares of the correlation coefficients for $NO_2$, $SO_2$, and HCHO were 0.92, 0.85, and 0.60, respectively. The larger errors of HCHO and $SO_2$ are mainly caused by the larger uncertainties of the DOAS fit and the





AMTD
6, 8129–8186, 2013



transformation of the light path length from 360 to 340 nm and 310 nm, respectively. The slopes of the regression lines for $NO_2$, $SO_2$, and HCHO are 0.85, 0.72, and 0.45, respectively. The positive intercepts of the fit curves show that the VMRs from LP-DOAS are generally larger than those from MAX-DOAS when the concentrations of the trace gases are relatively low. The reason for this difference is currently not clear, but may be caused by the different altitude ranges and horizontal distances, for which both methods are sensitive. The VMR from the rapid MAX-DOAS method represents the average between the ground and the sensitive altitude (typically < 200 m), while the LP-DOAS observations are representative for the trace gas VMR close to the surface. The rapid method usually integrates over horizontal distances of several km, while the LP-DOAS observations are representative for a light path of only 350 m.

In addition to the slopes and intercepts of the regression lines, we also calculated the average of the ratios (AR) and ratio of the average (RA) of all data pairs from MAX-DOAS and LP-DOAS data for each trace gas using Eqs. (11) and (12), respectively. The $NO_2$ AR and RA are 1.16 and 1.04, respectively. For $SO_2$, the AR and RA are 0.89 and 0.87, respectively. For HCHO, the AR and RA are 0.93 and 0.90, respectively. Like for the slopes of the regression lines, also these ratios are higher for $NO_2$ than for the other two trace gases. These findings indicate that the $NO_2$ profile probably has a steeper vertical gradient close to the surface than $SO_2$ and HCHO. Such differences in the vertical profiles can be expected close to strong emission sources due to the different atmospheric lifetimes (usually with the shortest lifetime for $NO_2$).

$$\mathrm{AR} = \frac{1}{n}\sum_{i=1}^{n}\frac{\mathrm{VMR}_{\mathrm{LP\text{-}DOAS}_i}}{\mathrm{VMR}_{\mathrm{MAX\text{-}DOAS}_i}} \tag{11}$$

$$\mathrm{RA} = \frac{\frac{1}{n}\sum_{i=1}^{n}\mathrm{VMR}_{\mathrm{LP\text{-}DOAS}_i}}{\frac{1}{n}\sum_{i=1}^{n}\mathrm{VMR}_{\mathrm{MAX\text{-}DOAS}_i}}. \tag{12}$$





AMTD
6, 8129–8186, 2013



In Eqs. (11) and (12), *n* indicates the number of hourly average VMR for each trace gas.

To study further the horizontal distribution of the observed trace gases, the statistical parameters of the linear regression curves of hourly average VMRs from LP-DOAS were compared with that from MAX-DOAS for each trace gas and the four AAs separately (Table 2). The ARs and RAs for the four AAs are also shown in the table. A detailed discussion for the different trace gases is presented in the sections below.

#### 4.3.1 Discussion for $NO_2$

For $NO_2$, the time series of average VMR mostly showed a slight "U" shape, which is probably mainly caused by the increased car traffic in the morning and evening (Fig. 18). On 21 May, the divergences of the VMR for the different AA are obvious. For example, the north VMR levels and fluctuations are mostly smaller than those of the other AA. The $NO_2$ emissions from the southeast urban source and air mass transport may have caused horizontal gradients. The presence of strong horizontal gradients is also indicated by the high temporal fluctuation of the LP-DOAS data. Air mass transport at night was relatively slow (Fig. 17b). Therefore, $NO_2$ could have increased and the horizontal gradients intensified, resulting in relatively large divergences in the morning. The decreased traffic and rapid air mass transport after approximately 10:00 LT may have decreased the divergences. During the afternoon, the increased traffic emissions may again have increased the divergences. The decrease in traffic flow may have alleviated the accumulation at night on weekends (3 June). Thus, a high $NO_2$ concentration is not observed in the morning on this day (Fig. 18). The slopes of the linear regression curves as well as ARs and RAs for 90 and 130° were smaller than that of 0 and 170° (Table 2). This result probably indicates that MAX-DOAS obtained higher $NO_2$ concentration in the south-east than in the other directions. This horizontal inhomogeneity was probably caused by the traffic emission in the urban center of Hefei City.





AMTD
6, 8129–8186, 2013



### 4.3.2 Discussion for $SO_2$

The east and south urban and industrial emissions from coal and petroleum combustion may have caused the obvious divergences of VMR levels and fluctuating amplitudes for the four azimuths, especially on 21 May. The smaller slopes, ARs, and RAs for 130 and 170° than that in the north direction also illustrate the effect of industrial emissions (Table 2). On 16 May and 3 June, $SO_2$ did not decrease during the morning. Especially on 16 May, the $SO_2$ VMRs are nearly similar for all directions, and the temporal variations are small (Figs. 19 and 21). Overall, the $SO_2$ observations show very similar spatial and temporal variations as the $NO_2$ observations indicating a common emission source.

### 4.3.3 Discussion for formaldehyde

Compared to $NO_2$ and $SO_2$, for HCHO the temporal variability and the differences between the different AAs are much smaller. This indicates that the horizontal gradients are in general smoother for HCHO. Increased divergences of the HCHO VMRs for the four azimuths are only found for 21 May (on that day also for $SO_2$ and $NO_2$ larger gradients were found). On 3 June, the HCHO concentrations continuously increased during the whole day. The VMRs for the four directions are nearly equivalent (Fig. 20) indicating that continuous HCHO emission occurred around the experiment site. Biomass burning that regularly occurs in farming areas around Hefei city during May and June (reported by newspapers: http://www.people.com.cn/h/2012/0614/c25408-3708357582.html) may have caused this result (de Smedt et al., 2010). HCHO is found in wood smoke based on the 1993 Environmental Protection Agency Report (Environmental Protection Agency, 1993). The smaller slopes, ARs, and RAs for 90 and 130° (Table 2) indicate that the emissions of the urban center may have slightly increased the ambient atmospheric HCHO concentration.





AMTD
6, 8129–8186, 2013



## 5 Retrieval of the surface aerosol extinction from the measured $O_4$ dSCD

Radiative transfer simulations show a clear relationship between the near-surface aerosol extinction and the $O_4$ dSCD for the 1° elevation angle (Fig. 23). This relationship depends on SZA (and also slightly on RAA). As expected, the vertical extension of the aerosol layer causes a relatively small uncertainty in this relationship, because the observations at 1° elevation angle are mainly sensitive for the atmospheric layers close to the surface. Thus, the aerosol extinction at the surface can be well retrieved from the measured $O_4$ dSCD using the rapid MAX-DOAS method. In Fig. 24 the aerosol extinction derived from the MAX-DOAS observations at 1° elevation angle are shown for the four days of the experiment. On 16 May and 3 June, rather low aerosol extinction is found; on the two other days, the values are systematically higher. These findings are in good agreement with the respective AOD values observed by MODIS (Fig. 15). In general also very good agreement between the results of the rapid method and the results from forward-scattering visibility meters is found. Here, however, it should be noted that no exact agreement can be expected because both measurements are based on different techniques and use different assumptions: the aerosol extinction from the visibility meters are derived from forward-scattered signal of a light-emitting diode of 950 nm. The results are converted to 550 nm using an empirical conversion formula (Nebuloni, 2005). It should also be noted that the detection limit of the visibility meters is about 0.15 $km^{-1}$. So after 11:00 LT on 16 May the true value of the aerosol extinction is probably lower than 0.15 $km^{-1}$.

Overall, the derived aerosol extinction values show similar spatial and temporal variation as the $NO_2$ and $SO_2$ VMR indicating a common emission source.

## 6 Error discussion

This section discusses the errors of the trace gas VMR and aerosol extinction derived from the rapid MAX-DOAS method. These errors are dominated by two main effects.





AMTD
6, 8129–8186, 2013



The first is the uncertainty of the DOAS fit. The second is the transformation from dSCD to average trace gas VMR or aerosol extinction near the ground.

The residual of the DOAS fit mainly contains noise and only some weak systematic structures. For $O_4$ and $NO_2$, the typical RMS was $6 \times 10^{-4}$, which corresponds to $O_4$ and $NO_2$ fitting errors of $1.4 \times 10^{42}$ molecules$^2$ cm$^{-5}$ and $8 \times 10^{14}$ molecules cm$^{-2}$, respectively. The typical RMS of the residual for the HCHO fit was $7 \times 10^{-4}$, corresponding to an error of the HCHO dSCD of $1.6 \times 10^{15}$ molecules cm$^{-2}$. The fitting window of $SO_2$ was close to the solar-blind region. Thus, the signal to noise ratio of the spectra was relatively low. In this case, the typical RMS of the residual was $1.2 \times 10^{-3}$, which corresponds to an error of the $SO_2$ dSCD of $2.2 \times 10^{15}$ molecules cm$^{-2}$. The uncertainty of the absorption cross-section of the trace gases, which depends on atmospheric temperature and pressure, may have contributed another 10 % relative error. Assuming average light path lengths, the resulting typical absolute and relative errors of the trace gas VMRs are: for $NO_2$: 0.14 ppb (or 15 %), for $SO_2$: 0.22 ppb (or 25 %), for HCHO: 0.14 ppb (or 18 %). The respective typical errors of the aerosol extinction are about 0.05 km$^{-1}$ or 15 %.

For the second process, one contribution to the uncertainty arises directly from the $O_4$ dSCD fitting error, which causes an error in the light path length of approximately 500 m. For relatively short path lengths, the relative contribution of this error increases. For example, relative errors of approximately 17 and 6 % were observed in the light path lengths of 3 and 9 km, respectively. Furthermore, the light path lengths for $SO_2$ and HCHO were obtained from those at 360 nm using Eqs. (7) and (8). The approximation from the standard deviations of the statistical parameters in Figs. 1 and 3 resulted in standard deviations of the light path lengths of 0.12 km at 310 nm and 0.04 km at 340 nm for light path lengths of 10 km at 360 nm.

Furthermore, in order to account for the different profile shapes of $O_4$ and the different trace gases, correction factors are used. Since the exact profile shapes of the trace gases and aerosols are usually unknown, we apply average correction factors, which might not be exactly appropriate for a given measurement. We estimate the corre-





AMTD
6, 8129–8186, 2013



sponding uncertainty from the spread of correction factors calculated for a large variety of assumed trace gas and aerosol profiles. The typical uncertainty is about 14 %. For high atmospheric visibility ($O_4$ dAMF > about 2) the uncertainties are usually smaller and for low atmospheric visibility ($O_4$ dAMF < about 1) the uncertainties can become substantially larger. It should be noted that for large SZA (larger than about 75°) the uncertainties related to the correction factors increase, Thus we recommend that the rapid method should be applied for SZA < 75°. In this study, the SZA was always < 60° and thus the resulting errors are usually rather small (similar to the DOAS fitting errors, see above). Depending on the atmospheric visibility and the analysed trace gas, the total uncertainty of the retrieved VMR is typically between 20 and 30 %. Here it should be noted that the uncertainties can become much larger in cases of very strong horizontal and/or vertical gradients, e.g. in close vicinity of very strong emission sources. In such cases, the proposed method should be used with caution. However, it should also be noted that in such situations the uncertainties of other methods (e.g. LP-DOAS) are usually large. Furthermore, in the presence of strong spatial gradients the representativeness of in-situ measurements is limited.

Future measurements might add in addition to the observations at 1° elevation angle also observation at a higher elevation angle (e.g. 2°) in order to derive information about the presence of very strong vertical gradients close to the surface (like the "collapsing criterium" used in Sinreich et al. (2013). Here it is important to note that these measurements at higher elevation angles could be performed with a coarser temporal resolution compared to the main observations at 1° elevation.

For the retrieval of the surface extinction, the errors caused by the missing knowledge of the aerosol profile (see Fig. 24) are usually rather small (typically about 0.05 or 10 % for aerosol extinctions between 0.1 and 1); they are similar to the uncertainties of the DOAS fit (see above).





AMTD
6, 8129–8186, 2013



## 7 Conclusions

We performed rapid measurements of surface-near trace gas VMR and aerosol extinction using MAX-DOAS measurements at 1° elevation angle. This method (for trace gases) was recently introduced by Sinreich et al. (2013), but we apply several important modifications: We restrict the measurements to 1° elevation angles, for which the uncertainty is usually much smaller than for higher elevation angles. The restriction to only one elevation angle also leads to a higher temporal and spatial resolution. We parameterise the calculated correction factors (and their uncertainties) as function of the simultaneously modelled $O_4$ dAMF. In this way the correction factors can be directly determined according to the retrieved $O_4$ dAMF of a given measurement. Finally, we extended the method to trace gases analysed at other wavelengths and to the determination of the surface near aerosol extinction.

The rapid method is based on the fact that for low elevation angles, the sensitivity of MAX-DOAS observations is high only for the layers close to the surface. For an elevation angle of 1° as used in this study, the altitude range, for which the measurement is sensitive for, is typically below 200 m (the so called sensitivity altitude range). Another important aspect of the rapid MAX-DOAS method is that the effective light path length can be determined from the measured absorption of the oxygen dimer $O_4$. Using this derived effective light path length, the trace gas dSCD can be transferred into average trace gas VMR or surface extinction, which are representative for the respective sensitivity altitude range corresponding to the atmospheric visibility of that measurement. Since the vertical profile shapes of $O_4$ and the other trace gases differ, correction factors have to be calculated and applied (Sinreich et al., 2013). Because these correction factors depend on the trace gas and aerosol profiles, we calculate mean values, as well as maximum and minimum values of the correction factors for various combinations of trace gas and aerosol profiles as function of the $O_4$ dAMF by RTM. We provide extended tables of these correction factors for different trace gases ($NO_2$ analysis at 360 nm, HCHO analysis at 340 nm, $SO_2$ analysis at 310 nm) and





AMTD
6, 8129–8186, 2013



a large variety of combinations of SZA and RAA (Table 2). These correction factors (and their uncertainties) are provided as function of the $O_4$ dAMF retrieved at 360 nm and can be used for (future) measurements by other groups using the same method. Based on RTM we estimate the typical uncertainty of the retrieved trace gas VMRs to 20 and 30 % (depending on the atmospheric visibility and the selected trace gas). Here it should be noted that in the presence of strong horizontal and/or vertical gradients, the uncertainties might be substantially larger.

As another important result of our study we found a clear relationship between the near-surface aerosol extinction and the $O_4$ dSCD for the 1° elevation angle. This indicates that also the average aerosol extinction close to the surface can be derived from the rapid MAX-DOAS method. Interestingly, the uncertainties of the retrieved surface aerosol extinction is usually smaller (typically about 15 %) than for the trace gas VMR, because only one inversion step is needed.

We applied the new method to MAX-DOAS measurements made in summer 2012 close to the city of Hefei. For that purpose we used a newly developed MAX-DOAS instrument (GM-DOAS), which can flexibly scan the atmosphere in two dimensions. For this study the GM-DOAS instrument made rapid measurements at 1° elevation and four azimuth angles (AA) (circularly pointed to 0, 90, 130, and 170°). In addition, spectra were taken at 90° elevation, which served as Fraunhofer reference spectra. Besides $O_4$, also dSCDs of $NO_2$, $SO_2$, and HCHO were analysed from the GM-DOAS measurements. Since the wavelength ranges of the $SO_2$ analysis (310 nm) and HCHO analysis (340 nm) differs from those of the $O_4$ and $NO_2$ analyses (360 nm), the effective light path length had to be extrapolated from 360 to 340 nm and 310 nm. This relationship between the light path lengths at the different wavelengths was established by RTM for 60 typical aerosol scenarios and various combinations of SZAs and RAAs. Second-order polynomial fits were constructed to extrapolate the light path lengths to 310 and 340 nm to accurately calculate the light path lengths for the determination of VMRs of $SO_2$ and HCHO.





AMTD
6, 8129–8186, 2013



We measured $NO_2$, $SO_2$, and HCHO VMRs and their horizontal distribution in the boundary layer near the Hefei City in China. To verify the reliability of the rapid MAX-DOAS method, the VMRs were compared with those from LP-DOAS. The results of the two techniques agree well. The squares of the correlation coefficients for $NO_2$, $SO_2$, and HCHO were 0.92, 0.85, and 0.60, respectively. Usually the results for the four AAs were found to be very similar. However, in some cases, also significant differences occurred, which indicates horizontal gradients of the trace gas concentrations close to the surface near the experiment site. This result was probably caused by industrial and urban emissions. Results for $NO_2$ VMR, $SO_2$ VMR and surface aerosol extinction showed very similar spatial-temporal variation indicating common sources. Interestingly, for the day with the strongest divergence between the different AAs, also the strongest temporal variations of the trace gas VMRs were found in the LP-DOAS measurements.

We also determined the aerosol extinction close to the surface from the rapid MAX-DOAS method. The results from MAX-DOAS agree well with the AOD values observed by MODIS and the results (at 550 nm) derived from forward-scattering visibility meters.

In summary, the novel analysis technique together with the newly developed 2-D MAX-DOAS instrument can rapidly monitor the horizontal distribution of average trace gases VMR and aerosol extinction in the boundary layer. The results provide important information for the analysis of emission sources, transport, and atmospheric chemical reactions of trace gases.

**Supplementary material related to this article is available online at http://www.atmos-meas-tech-discuss.net/6/8129/2013/amtd-6-8129-2013-supplement.zip.**





AMTD
6, 8129–8186, 2013



*Acknowledgements.* This work was supported by the Special Project of Environmental Nonprofit Industry Research, China (Grant No: 201109007) and National Natural Science Foundation of China (Grant No.: 41275038). We are very thankful to Rainer Volkamer and Roman Sinreich for their feedback to our study and the fruitful discussions.

## References

Bobrowski, N., Honninger, G., Galle, B., and Platt, U.: Detection of bromine monoxide in a vol-canic plume, Nature, 423, 273–276, 2003.

Bogumil, K., Orphal, J., Homann, T., Voigt, S., Spietz, P., Fleischmann, O. C., Vogel, A., Hartmann, M., Kromminga, H., Bovensmann, H., Frerick, J., and Burrows, J. P.: Measurements of molecular absorption spectra with the SCIAMACHY pre-flight model: instrument characterization and reference data for atmospheric remote-sensing in the 230–2380 nm region, J. Photoch. Photobio. A, 157, 167–184, 2003.

Bovensmann, H., Burrows, J. P., Buchwitz, M., Frerick, J., Noël, S., Rozanov, V. V., Chance, K. V., and Goede, A. H. P.: SCIAMACHY – mission objectives and measurement modes, J. Atmos. Sci., 56, 127–150, 1999.

Brühl, C. and Crutzen, P. J.: MPIC two-dimensional model, in: The Atmospheric Effect of Stratospheric Aircraft, 1292, edited by: Prather, M. J. and Remsberg, E. E., NASA Ref. Publications, 103–104, 1993.

Burrows, J. P., Weber, M., Buchwitz, M., Rozanov, V. V., Ladstätter-Weißenmayer, A., Richter, A., DeBeek, R., Hoogen, R., Brmstedt, K., and Eichmann, K. U.: The global ozone monitoring experiment (GOME): mission concept and first scientific results, J. Atmos. Sci., 56, 151–175, 1999.

Burrows, J. P., Platt, U., and Borrell, P. (Eds.): The Remote Sensing of Tropospheric Composition from Space, http://www.ppmborrell.co.uk/RemoteSensingBook/, last access: 29 August 2013, Springer-Verlag, Berlin, Heidelberg, 2011.

Clemer, K., Fayt, C., Hendrick, F., Hermans, C., Pinardi, G., and Van Roozendael, M.: The simultaneous retrieval of tropospheric aerosol extinction and $NO_2$ vertical profiles from MAX-DOAS measurements in Beijing, in: Proceedings of the 8th International Symposium on Tropospheric Profiling, 19–23 October 2009, Delft, the Netherlands, 2009.





AMTD

6, 8129–8186, 2013



Clémer, K., Van Roozendael, M., Fayt, C., Hendrick, F., Hermans, C., Pinardi, G., Spurr, R., Wang, P., and De Mazière, M.: Multiple wavelength retrieval of tropospheric aerosol optical properties from MAXDOAS measurements in Beijing, Atmos. Meas. Tech., 3, 863–878, doi:10.5194/amt-3-863-2010, 2010.

Crutzen, P. J.: The role of NO and $NO_2$ in the chemistry of the troposphere and stratosphere, Annu. Rev. Earth Planet. Sci., 7, 443–472, 1979.

De Smedt, I., Stavrakou, T., Müller, J. F., Van Der A, R. J., and Van Roozendael, M.: Trend detection in satellite observations of formaldehyde tropospheric columns, Geophys. Res. Lett., 37, L18808, doi:10.1029/2010GL044245, 2010.

Environmental Protection Agency: A Summary of the Emissions Characterization and Non-cancer Respiratory Effects of Wood Smoke, EPA-453/R-93-036, http://burningissues.org/table2.htm (last access: 28 August 2013), 1993.

Environmental Protection Agency: National air quality and emissions trends report 1998, Rep. EPA 454/R-00-003, The United Station, 1998.

Eskes, H. J. and Boersma, K. F.: Averaging kernels for DOAS total-column satellite retrievals, Atmos. Chem. Phys., 3, 1285–1291, doi:10.5194/acp-3-1285-2003, 2003.

Fayt, C. and van Roozendael, M.: WinDOAS 2.1 Software User Manual, IASB/BIRA, http://uv-vis.aeronomie.be/software/WinDOAS/WinDOAS-SUM-210b.pdf (last access: 28 August 2013), 2009.

Frieß, U., Sihler, H., and Sander, R.: The vertical distribution of BrO and aerosols in the Arctic: Measurements by active and passive differential optical absorption spectroscopy, J. Geophys. Res., 116, D00R04, doi:10.1029/2011JD015938, 2011.

Frins, E., Bobrowski, N., Platt, U., and Wagner, T.: Tomographic MAX-DOAS observations of sun-illuminated targets: a new technique providing well defined absorption paths in the boundary layer, Appl. Optics, 45, 6227, doi:10.1364/AO.45.006227, 2006.

Frins, E., Platt, U., and Wagner, T.: High spatial resolution measurements of $NO_2$ applying Topographic Target Light scattering-Differential Optical Absorption Spectroscopy (ToTaL-DOAS), Atmos. Chem. Phys., 8, 7595–7601, doi:10.5194/acp-8-7595-2008, 2008.

Grainger, J. F. and Ring, J.: Anomalous Fraunhofer line profiles, Nature, 193, p. 762, 1962.

Greenblatt, G. D., Orlando, J. J., Burkholder, J. B., and Ravishankara, A. R.: Absorption measurements of oxygen between 330 and 1140 nm, J. Geophys. Res., 95, 18577–18582, 1990.





AMTD
6, 8129–8186, 2013



Heckel, A., Richter, A., Tarsu, T., Wittrock, F., Hak, C., Pundt, I., Junkermann, W., and Burrows, J. P.: MAX-DOAS measurements of formaldehyde in the Po-Valley, Atmos. Chem. Phys., 5, 909–918, doi:10.5194/acp-5-909-2005, 2005.

Hellén, H., Hakola, H., Reissell, A., and Ruuskanen, T. M.: Carbonyl compounds in boreal coniferous forest air in Hyytiälä, Southern Finland, Atmos. Chem. Phys., 4, 1771–1780, doi:10.5194/acp-4-1771-2004, 2004.

Hess, M., Koepke, P., and Schult, I.: Optical Properties of Aerosols and Clouds: The Software Package OPAC, Vol. 79, No. 5, http://ether.ipsl.jussieu.fr/etherTypo/?id=1058 (last access: 28 August 2013), May 1998.

Ho, K. F., Lee, S. C., Louie, P. K. K., and Zou, S. C.: Seasonal variation of carbonyl compound concentrations in urban area of Hong Kong, Atmos. Environ., 36, 1259–1265, 2002.

Hönninger, G., von Friedeburg, C., and Platt, U.: Multi axis differential optical absorption spectroscopy (MAX-DOAS), Atmos. Chem. Phys., 4, 231–254, doi:10.5194/acp-4-231-2004, 2004.

Irie, H., Takashima, H., Kanaya, Y., Boersma, K. F., Gast, L., Wittrock, F., Brunner, D., Zhou, Y., and Van Roozendael, M.: Eight-component retrievals from ground-based MAX-DOAS observations, Atmos. Meas. Tech., 4, 1027–1044, doi:10.5194/amt-4-1027-2011, 2011.

Johansson, M., Galle, B., Yu, T., Tang, L., Chen, D., Li, H., Li, J. X., and Zhang, Y.: Quantification of total emission of air pollutants from Beijing using mobile mini-DOAS, Atmos. Environ., 42, 6926–6933, 2008.

Johansson, M., Rivera, C., de Foy, B., Lei, W., Song, J., Zhang, Y., Galle, B., and Molina, L.: Mobile mini-DOAS measurement of the outflow of $NO_2$ and HCHO from Mexico City, Atmos. Chem. Phys., 9, 5647–5653, doi:10.5194/acp-9-5647-2009, 2009.

Kraus, S.: DOASIS, A Framework Design for DOAS, http://hci.iwr.uni-heidelberg.de/publications/dip/2006/Kraus_PhD2006.pdf, PhD-thesis, University of Mannheim, 2006.

Li, X., Brauers, T., Shao, M., Garland, R. M., Wagner, T., Deutschmann, T., and Wahner, A.: MAX-DOAS measurements in southern China: retrieval of aerosol extinctions and validation using ground-based in-situ data, Atmos. Chem. Phys., 10, 2079–2089, doi:10.5194/acp-10-2079-2010, 2010.

Li, X., Brauers, T., Hofzumahaus, A., Lu, K., Li, Y. P., Shao, M., Wagner, T., and Wahner, A.: MAX-DOAS measurements of $NO_2$, HCHO and CHOCHO at a rural site in Southern China, Atmos. Chem. Phys., 13, 2133–2151, doi:10.5194/acp-13-2133-2013, 2013.





AMTD
6, 8129–8186, 2013



Lurmann, F. W. and Main, H. H.: Analysis of the ambient VOC data collected in the Southern California Air Quality Study, Final Report, ARB Contract NO.A832-130, California Air Resources Board, Scaramento, CA, USA, 1992.

Martin, R. V., Chance, K., Jacob, D. J., Kurosu, T. P., Spurr, R. J. D., Bucsela, E., Gleason, J. F., Palmer, P. I., Bey, I., Fiore, A. M., Li, Q., Yantosca, R. M., and Koelemeijer, R. B. A.: An Improved Retrieval of Tropospheric Nitrogen Dioxide from GOME, J. Geophys. Res., 107, 4437, doi:10.1029/2001JD001027, 2002.

Meller, R. and Moortgat, G. K.: Temperature dependence of the absorption cross sections of formaldehyde between 223 and 323 K in the wavelength range 225–375 nm, J. Geophys. Res., 105, 7089–7101, 2000.

National Aeronautics and Space Administration: Daily MODIS Level 3 Atmosphere Products, http://modis.gsfc.nasa.gov/data/dataprod/dataproducts.php?MOD_NUMBER=08, last access: 26 November 2012.

Nebuloni, R.: Empirical relationships between extinction coefficient and visibility in fog, Appl. Optics, 44, 3795, doi:10.1364/AO.44.003795, 2005.

Pikelnaya, O., Hurlock, S. C., Trick, S., and Stutz, J.: Intercomparison of multiaxis and long-path optical absorption spectroscopy measurements in the marine boundary layer, J. Geophys. Res., 112, D10S01, doi:10.1029/2006JD007727, 2007.

Platt, U. and Stutz, J.: Differential Optical Absorption Spectroscopy, Springer-Verlag, Heidelberg, Berlin, 229–375, 2008.

Qin, M., Xie, P. H., Liu, W. Q., Li, A., Dou, K., Fang, W., Liu, J. G., and Zhang, W. J.: Observation of atmospheric nitrous acid with DOAS in Beijing, China, J. Environ. Sci., 18, 69–75, 2006.

Rozanov, A., Rozanov, V., Buchwitz, M., Kokhanovsky, A., and Burrows, J.: SCIATRAN 2.0 – A new radiative transfer model for geophysical applications in the 175–2400 nm spectral region, in: Atmospheric Remote Sensing: Earth's Surface, Troposphere, Stratosphere and Mesosphere – I, edited by: Burrows, J. and Eichmann, K., Adv. Space Res., 36, 1015–1019, doi:10.1016/j.asr.2005.03.012, 2005.

Richter, A. and Wagner, T.: The Use of UV, Visible and Near IR Solar Back Scattered Radiation to Determine Trace Gases, in: The Remote Sensing of Tropospheric Composition from Space, edited by: Burrows, J. P., Platt, U., and Borrell, P., Springer, Heidelberg, 67–122, doi:10.1007/978-3-642-14791-3, 2011.

Seinfeld, J. H. and Pandis, S. N.: Atmospheric Chemistry and Physics – From Air Pollution to Climate Change, John Wiley, New York, 1998.





AMTD
6, 8129–8186, 2013



Sinreich, R., Volkamer, R., Filsinger, F., Frieß, U., Kern, C., Platt, U., Sebastián, O., and Wagner, T.: MAX-DOAS detection of glyoxal during ICARTT 2004, Atmos. Chem. Phys., 7, 1293–1303, doi:10.5194/acp-7-1293-2007, 2007.

Sinreich, R., Merten, A., Molina, L., and Volkamer, R.: Parameterizing radiative transfer to convert MAX-DOAS dSCDs into near-surface box-averaged mixing ratios, Atmos. Meas. Tech., 6, 1521–1532, doi:10.5194/amt-6-1521-2013, 2013.

Smith, S. J., van Aardenne, J., Klimont, Z., Andres, R. J., Volke, A., and Delgado Arias, S.: Anthropogenic sulfur dioxide emissions: 1850–2005, Atmos. Chem. Phys., 11, 1101–1116, doi:10.5194/acp-11-1101-2011, 2011.

Solomon, S., Schmeltekopf, A. L., and Sanders, R. W.: On the interpretation of zenith sky absorption measurements, J. Geophys. Res., 92, 8311–8319, 1987.

Theys, N., Van Roozendael, M., Hendrick, F., Fayt, C., Hermans, C., Baray, J.-L., Goutail, F., Pommereau, J.-P., and De Mazière, M.: Retrieval of stratospheric and tropospheric BrO columns from multi-axis DOAS measurements at Reunion Island (21° S, 56° E), Atmos. Chem. Phys., 7, 4733–4749, doi:10.5194/acp-7-4733-2007, 2007.

Vandaele, A. C., Hermans, C., Simon, P. C., Carleer, M., Colin, R., Fally, S., Mérienne, M.-F., Jenouvrier, A., and Coquart, B.: Measurements of the $NO_2$ absorption cross section from 42000 $cm^{-1}$ to 10000 $cm^{-1}$ (238–1000 nm) at 220 K and 294 K, J. Quant. Spectrosc. Ra., 59, 171–184, 1998.

Vlemmix, T., Piters, A. J. M., Stammes, P., Wang, P., and Levelt, P. F.: Retrieval of tropospheric $NO_2$ using the MAX-DOAS method combined with relative intensity measurements for aerosol correction, Atmos. Meas. Tech., 3, 1287–1305, doi:10.5194/amt-3-1287-2010, 2010.

Vlemmix, T., Piters, A. J. M., Berkhout, A. J. C., Gast, L. F. L., Wang, P., and Levelt, P. F.: Ability of the MAX-DOAS method to derive profile information for $NO_2$: can the boundary layer and free troposphere be separated?, Atmos. Meas. Tech., 4, 2659–2684, doi:10.5194/amt-4-2659-2011, 2011.

Wagner, T., von Friedeburg, C., Wenig, M., Otten, C., and Platt, U.: UV/vis observations of atmospheric $O_4$ absorptions using direct moon light and zenith scattered sunlight under clear and cloudy sky conditions, J. Geophys. Res., 107, D204424, doi:10.1029/2001JD001026, 2002.

Wagner, T., Beirle, S., Deutschmann, T., Eigemeier, E., Frankenberg, C., Grzegorski, M., Liu, C., Marbach, T., Platt, U., and Penning de Vries, M.: Monitoring of atmospheric trace gases,





AMTD
6, 8129–8186, 2013



clouds, aerosols and surface properties from UV/vis/NIR satellite instruments, J. Opt. A, 10, 104019, doi:10.1088/1464-4258/10/10/104019, 2008.
Wagner, T., Beirle, S., and Deutschmann, T.: Three-dimensional simulation of the Ring effect in observations of scattered sun light using Monte Carlo radiative transfer models, Atmos. Meas. Tech., 2, 113–124, doi:10.5194/amt-2-113-2009, 2009.
Wagner, T., Ibrahim, O., Shaiganfar, R., and Platt, U.: Mobile MAX-DOAS observations of tropospheric trace gases, Atmos. Meas. Tech., 3, 129–140, doi:10.5194/amt-3-129-2010, 2010.
Wagner, T., Beirle, S., Brauers, T., Deutschmann, T., Frieß, U., Hak, C., Halla, J. D., Heue, K. P., Junkermann, W., Li, X., Platt, U., and Pundt-Gruber, I.: Inversion of tropospheric profiles of aerosol extinction and HCHO and $NO_2$ mixing ratios from MAX-DOAS observations in Milano during the summer of 2003 and comparison with independent data sets, Atmos. Meas. Tech., 4, 2685–2715, doi:10.5194/amt-4-2685-2011, 2011.
Wang, Y., Li, A., and Xie, P. H.: Measurements of $NO_2$ mixing ratios with topographic target light scattering-differential optical absorption spectroscopy system and comparisons to point monitoring technique, Chin. Phys. B, 21, 114211, 2012.
Wittrock, F., Oetjen, H., Richter, A., Fietkau, S., Medeke, T., Rozanov, A., and Burrows, J. P.: MAX-DOAS measurements of atmospheric trace gases in Ny-Ålesund – Radiative transfer studies and their application, Atmos. Chem. Phys., 4, 955–966, doi:10.5194/acp-4-955-2004, 2004.
Wu, F. C., Xie, P. H., Li, A., Chan, K. L., Hartl, A., Wang, Y., Si, F. Q., Zeng, Y., Qin, M., Xu, J., Liu, J. G., Liu, W. Q., and Wenig, M.: Observations of $SO_2$ and $NO_2$ by mobile DOAS in the Guangzhou Eastern Area during the Asian Games 2010, Atmos. Meas. Tech. Discuss., 6, 261–301, doi:10.5194/amtd-6-261-2013, 2013.
Yilmaz, S.: Retrieval of Atmospheric Aerosol and Trace Gas Vertical Profiles using Multi-Axis Differential Optical Absorption Spectroscopy, Dissertation submitted to the Combined Faculties for the Natural Sciences and for Mathematics of the Ruperto-Carola University of Heidelberg, Germany for the degree of Doctor of Natural Sciences, 2012.





AMTD
6, 8129–8186, 2013



**Table 1.** Parameters for 60 chosen aerosol scenarios.

| Parameter | Values |
|---|---|
| aerosol optical depth ($\tau$) | 0.1, 0.3, 0.5, 0.7, 0.9, 1.1, 1.3, 1.5, 1.7, 2.0 |
| fraction ($F$) of $\tau$in the boundary layer | 0.8 |
| height ($H$) of the boundary layer | 0.5, 0.8, 1.1, 1.4, 1.7, 1.9 |





AMTD
6, 8129–8186, 2013



**Table 2.** Statistical parameters of the correlation between LP-DOAS and MAX-DOAS for four AAs and each trace gas.

| Statistical parameters | 0° | 90° | 130° | 170° |
|---|---|---|---|---|
| | | $NO_2$ | | |
| $R^2$ | 0.84 | 0.59 | 0.87 | 0.90 |
| intercept | 1.20 | 0.82 | 1.04 | 1.34 |
| slope | 0.86 | 0.78 | 0.75 | 0.78 |
| AR | 1.35 | 1.06 | 1.09 | 1.35 |
| RA | 1.12 | 0.99 | 0.98 | 1.06 |
| | | $SO_2$ | | |
| $R^2$ | 0.74 | 0.70 | 0.79 | 0.73 |
| intercept | 1.23 | 0.91 | 0.98 | 1.50 |
| slope | 0.64 | 0.73 | 0.64 | 0.58 |
| AR | 0.93 | 0.97 | 0.85 | 0.94 |
| RA | 0.88 | 0.93 | 0.81 | 0.85 |
| | | HCHO | | |
| $R^2$ | 0.46 | 0.23 | 0.52 | 0.62 |
| intercept | 1.67 | 2.00 | 1.54 | 1.27 |
| slope | 0.37 | 0.25 | 0.39 | 0.50 |
| AR | 0.99 | 0.95 | 0.94 | 0.93 |
| RA | 0.91 | 0.89 | 0.88 | 0.90 |





AMTD
6, 8129–8186, 2013



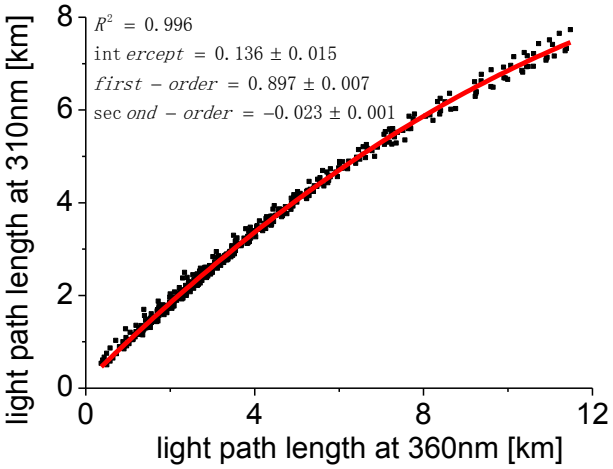


**Fig. 1.** Scatter plot of light path lengths at 310 nm against light path lengths at 360 nm for 60 aerosol scenarios and combinations of three SZAs and RAAs. The statistical parameters derived from a second-order polynomial fitted to the simulation results are also shown.





AMTD
6, 8129–8186, 2013



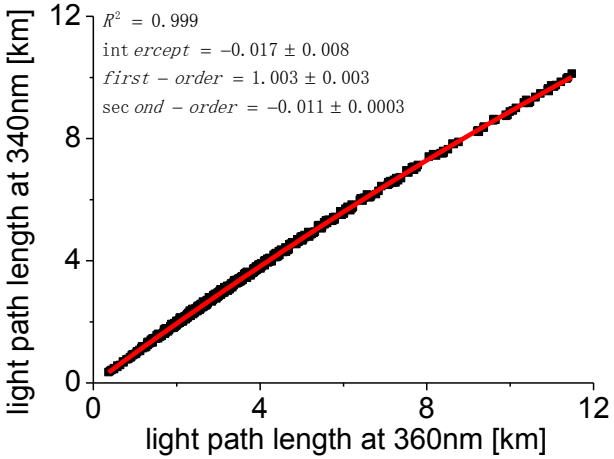


**Fig. 2.** Scatter plot of light path lengths at 340 nm against light path lengths at 360 nm for 60 aerosol scenarios and combinations of three SZAs and RAAs. The statistical parameters derived from a second-order polynomial fitted to the simulation results are also shown.





AMTD
6, 8129–8186, 2013



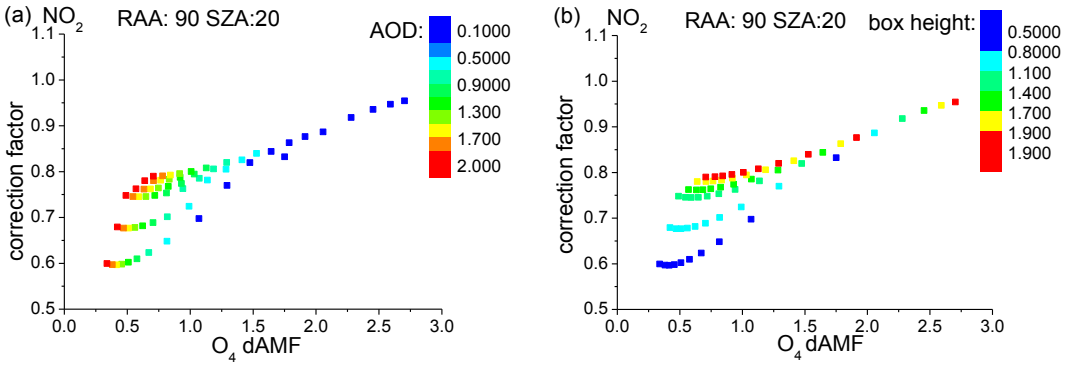


**Fig. 3.** Correction factors for a trace gas box profile (1 km) as function of the $O_4$ dAMF calculated for 60 different aerosol scenarios (see Table 1). The colors indicate the AOD **(a)** and aerosol layer height **(b)**. Calculations are performed for 360 nm and for a RAA of 90° and SZA of 20°.





AMTD
6, 8129–8186, 2013



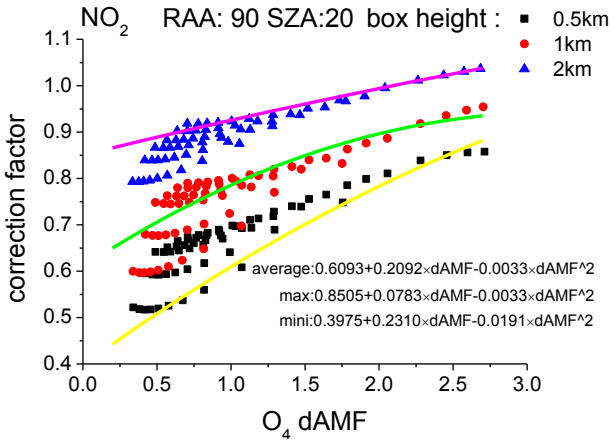


**Fig. 4.** Correction factors for trace gas box profiles of 0.5, 1 and 2 km as well as for the 60 aerosol scenarios (Table 1) as function of the $O_4$ dAMF. The green line indicates the average fitted polynomial, the magenta and yellow lines indicate polynomial fits to the maxima and minima, respectively. Calculations are performed for 360 nm and for a RAA of 90° and SZA of 20°.





AMTD
6, 8129–8186, 2013



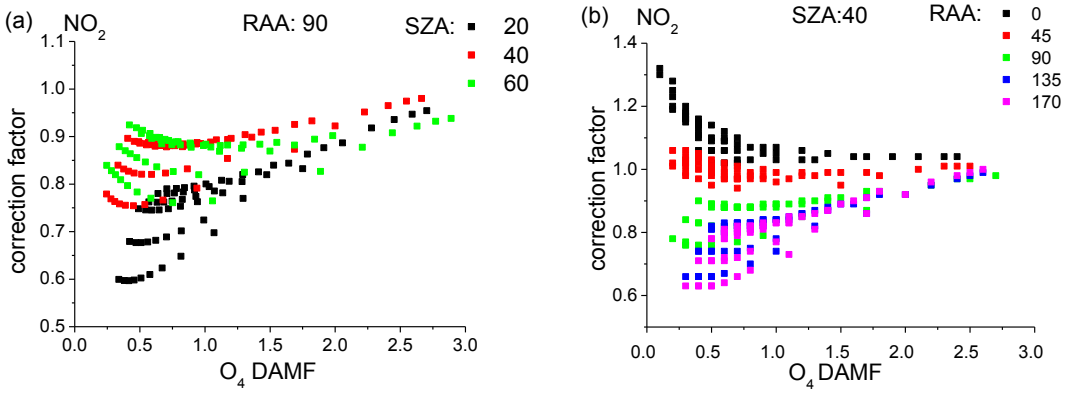


**Fig. 5.** Correction factors for a trace gas box profile (1 km) as function of the $O_4$ dAMF **(a)** for RAA of 90 and SZAs of 20, 40 and 60°, **(b)** for SZA of 40 and RAAS of 0, 45, 90, 135 and 180°.





AMTD
6, 8129–8186, 2013



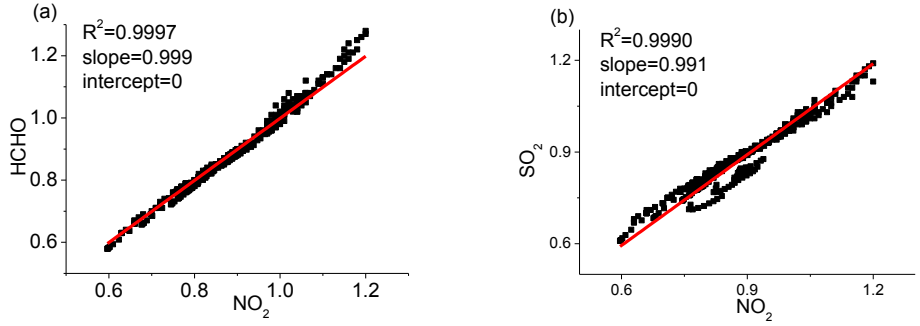


**Fig. 6.** Correlations of correction factors for the HCHO analysis at 340 nm **(a)** and the $SO_2$ analysis at 310 nm **(b)** versus those for $NO_2$ at 360 nm.





AMTD
6, 8129–8186, 2013



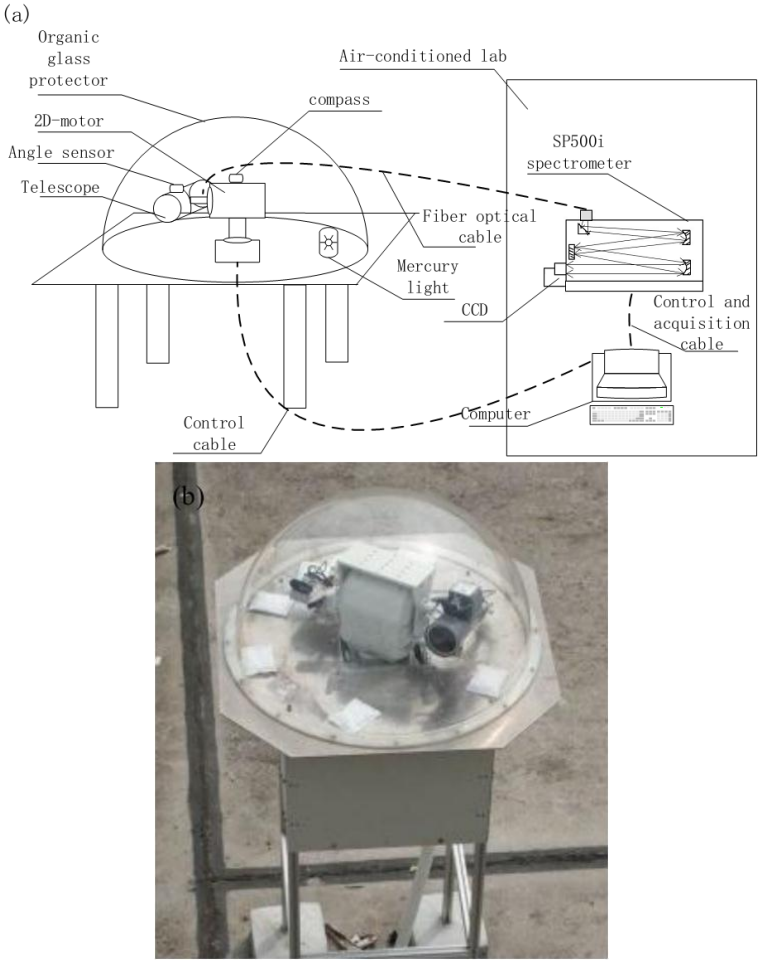


**Fig. 7.** Schematic drawing **(a)** and photograph **(b)** of the GM-DOAS instrument.





AMTD
6, 8129–8186, 2013

A rapid method to derive horizontal distributions of trace gases and aerosols

Y. Wang et al.



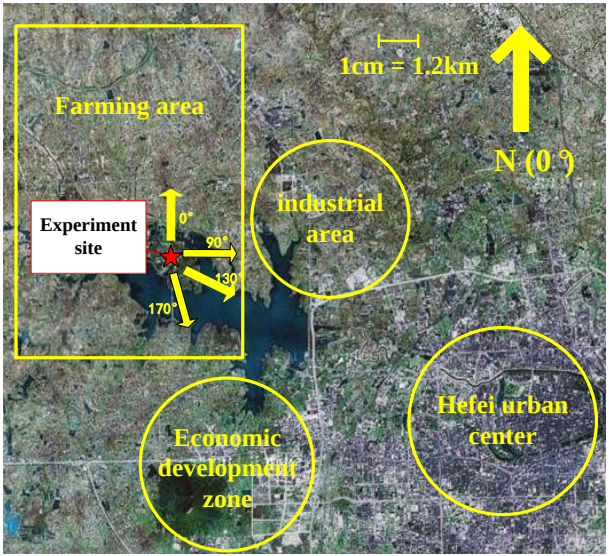


**Fig. 8.** Experiment site was located approximately 6 km away from the downtown in the west-north outskirts of Hefei City. The four AAs point to a farming area, an industrial area, an urban center, and an economic development zone. The GM-DOAS and LP-DOAS instruments were located at the experiment site. The distance between the two instruments was less than 100 m.





AMTD
6, 8129–8186, 2013



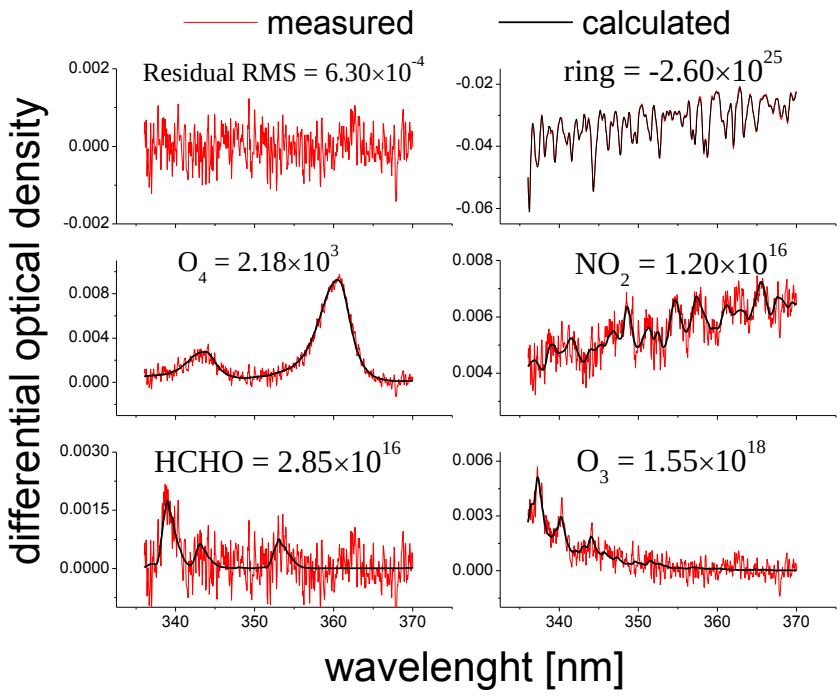


**Fig. 9.** Example of a DOAS fit of $O_4$ and $NO_2$ at 12:45 LT on 16 May 2012. The Fraunhofer reference spectrum used was the latest 90° spectrum before the measurement. The results were as follows: $dSCD(O_4) = (2.18 \pm 0.14) \times 10^{43}$ molecules$^2$ cm$^{-5}$, and $dSCD(NO_2) = (1.2 \pm 0.08) \times 10^{16}$ molecules cm$^{-2}$. The RMS of the residual was $6.3 \times 10^{-4}$.





AMTD
6, 8129–8186, 2013

A rapid method to derive horizontal distributions of trace gases and aerosols

Y. Wang et al.



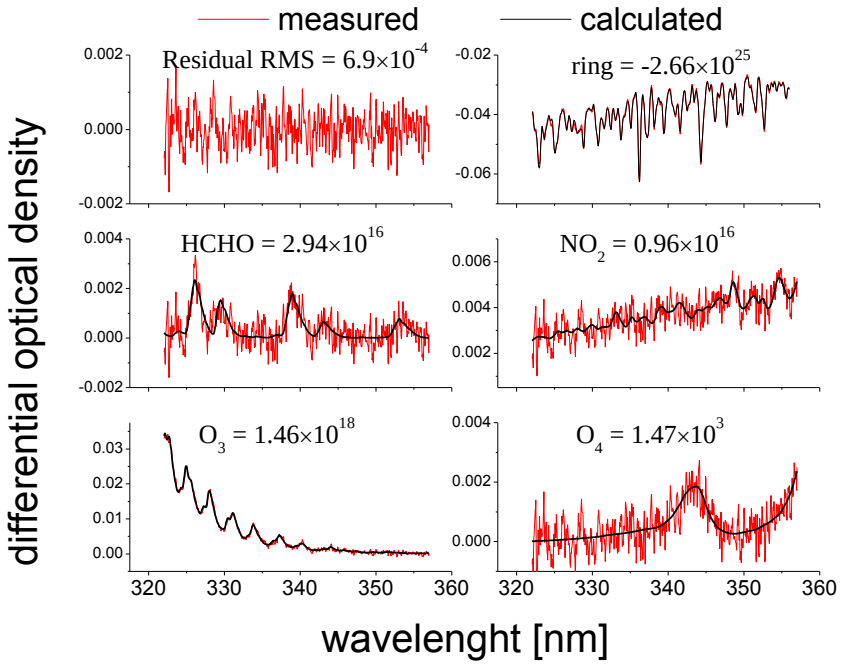


**Fig. 10.** Example of a DOAS fit of HCHO at 12:45 LT on 16 May 2012. The Fraunhofer reference spectrum used was the latest 90° spectrum before the measurement. The derived HCHO dSCD was $(2.94 \pm 0.16) \times 10^{16}$ molecules cm$^{-2}$. The RMS of the residual was $6.9 \times 10^{-4}$.





AMTD
6, 8129–8186, 2013



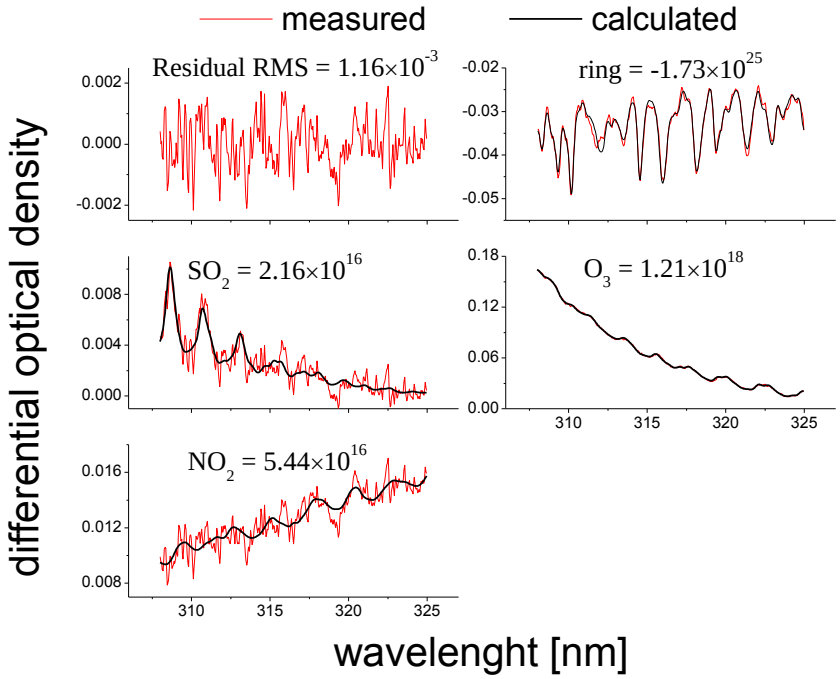


**Fig. 11.** Example of a DOAS fit of $SO_2$ at 12:45 LT on 16 May 2012. The Fraunhofer reference spectrum used was the latest 90° spectrum before the measurement. The derived $SO_2$ dSCD was $(2.16 \pm 0.22) \times 10^{16}$ molecules cm$^{-2}$. The RMS of the residual was $1.16 \times 10^{-3}$.





AMTD
6, 8129–8186, 2013



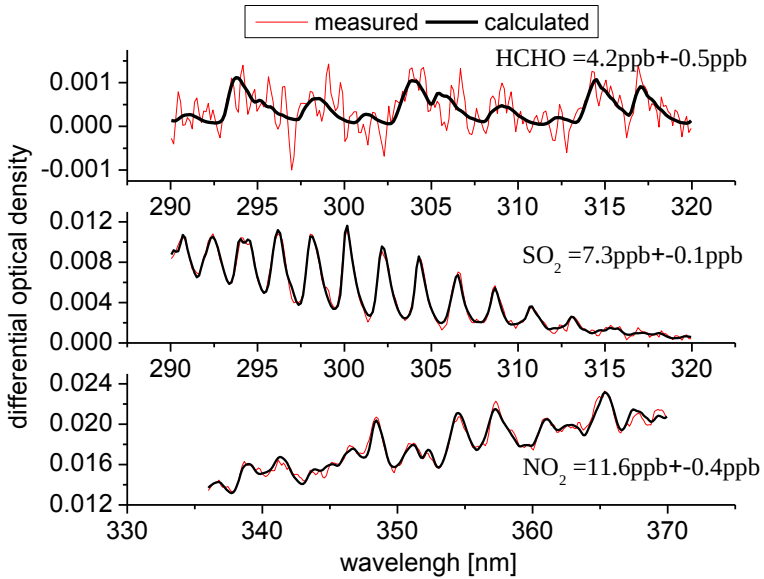


**Fig. 12.** Example of LP-DOAS fits of HCHO, $SO_2$, and $NO_2$ at 09:05 LT on 18 May 2012. The results are as follows: VMR (HCHO) = 4.2 ± 0.5 ppb, VMR ($SO_2$) = 7.3 ± 0.1 ppb, and VMR ($NO_2$) = 11.6 ± 0.4 ppb.





AMTD
6, 8129–8186, 2013



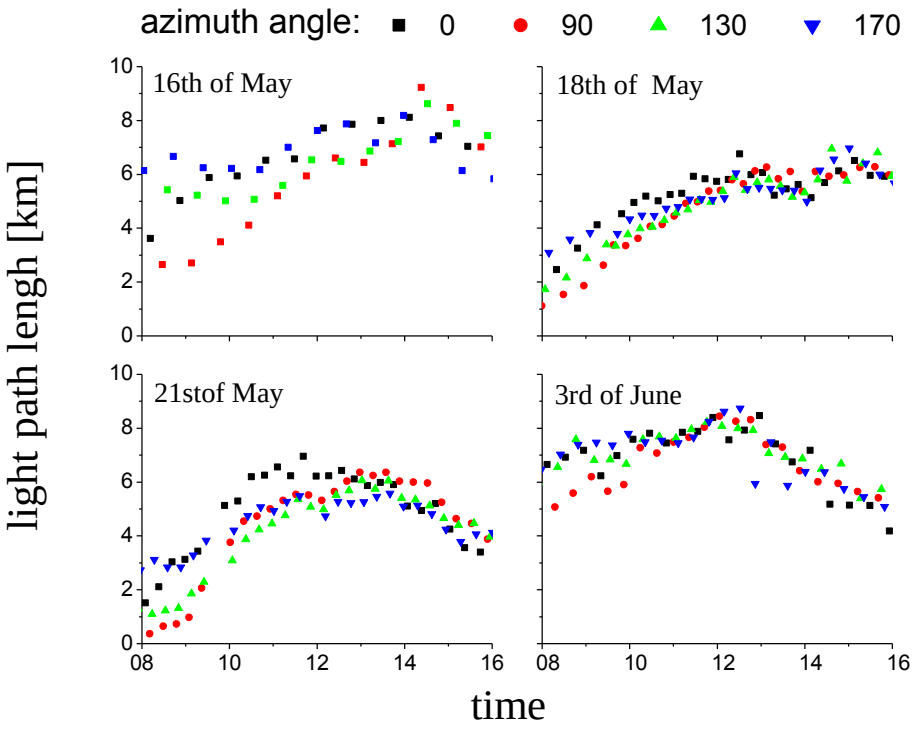


**Fig. 13.** Effective light path lengths at 360 nm near the ground for observations at 1° elevation angle during four selected days. The black, red, green, and blue dots correspond to the 0° (north), 90° (east), 130° (east-south), and 170° (south) AAs.





AMTD
6, 8129–8186, 2013



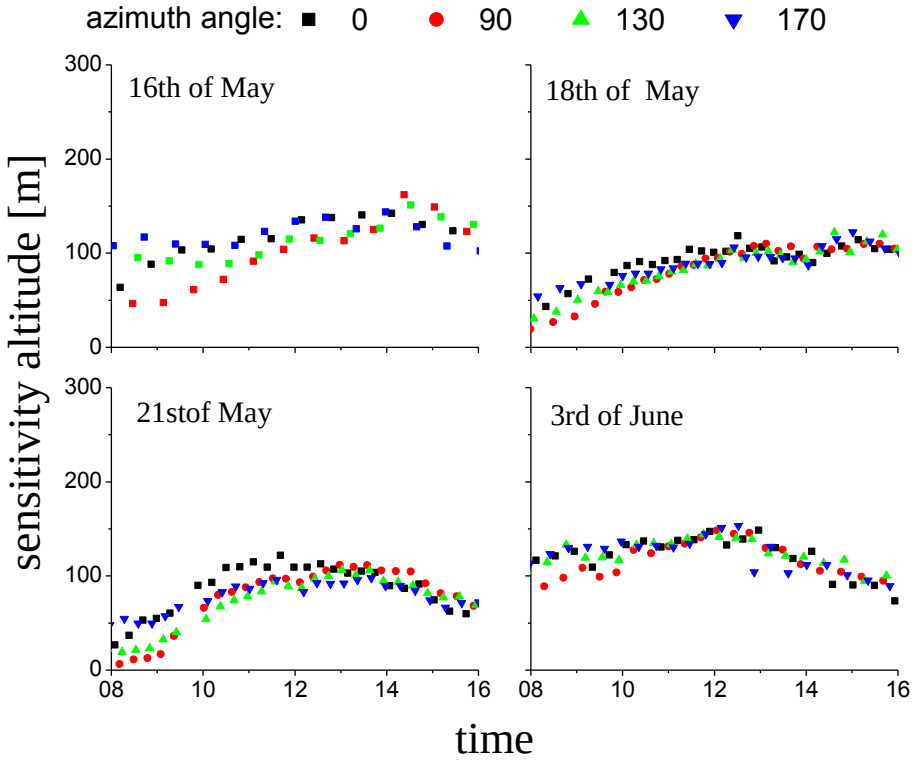


**Fig. 14.** Time series of the sensitive altitude ranges at 360 nm.





AMTD
6, 8129–8186, 2013

A rapid method to derive horizontal distributions of trace gases and aerosols

Y. Wang et al.



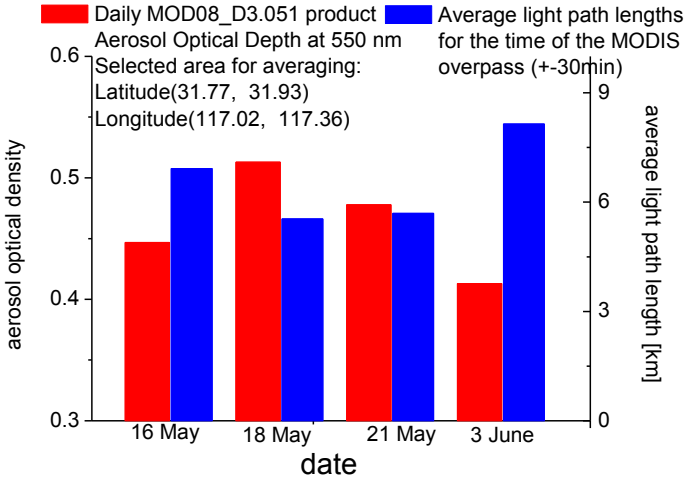


**Fig. 15.** Comparison of AOD (red bars) near the experimental site from the daily data of MODIS Level 3 Atmosphere Products (MOD 08_D3) and the average light path lengths (blue bars) for the time of the MODIS overpass (± 30 min).





AMTD
6, 8129–8186, 2013



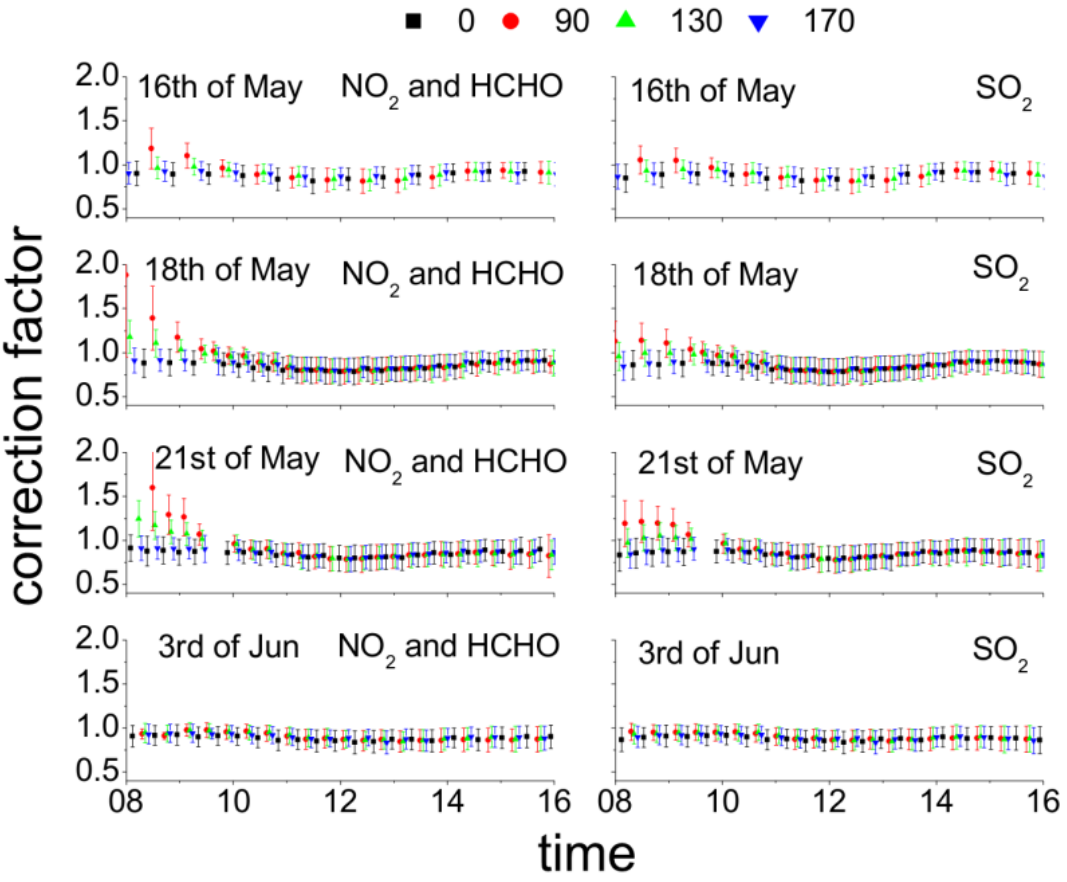


**Fig. 16.** Time series of the average correction factors and their corresponding uncertainties for $NO_2$, HCHO and $SO_2$ for four azimuth angles during the period of the experiment.





AMTD
6, 8129–8186, 2013



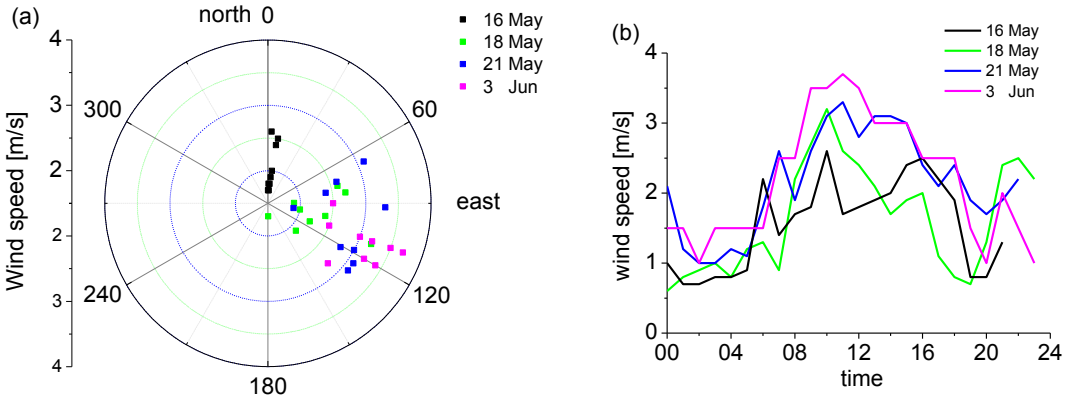


**Fig. 17.** Wind direction and speed on 16, 18, and 21 May and 3 June 2012. **(a)** Wind direction rose map and **(b)** time series of hourly average wind speed.





AMTD
6, 8129–8186, 2013



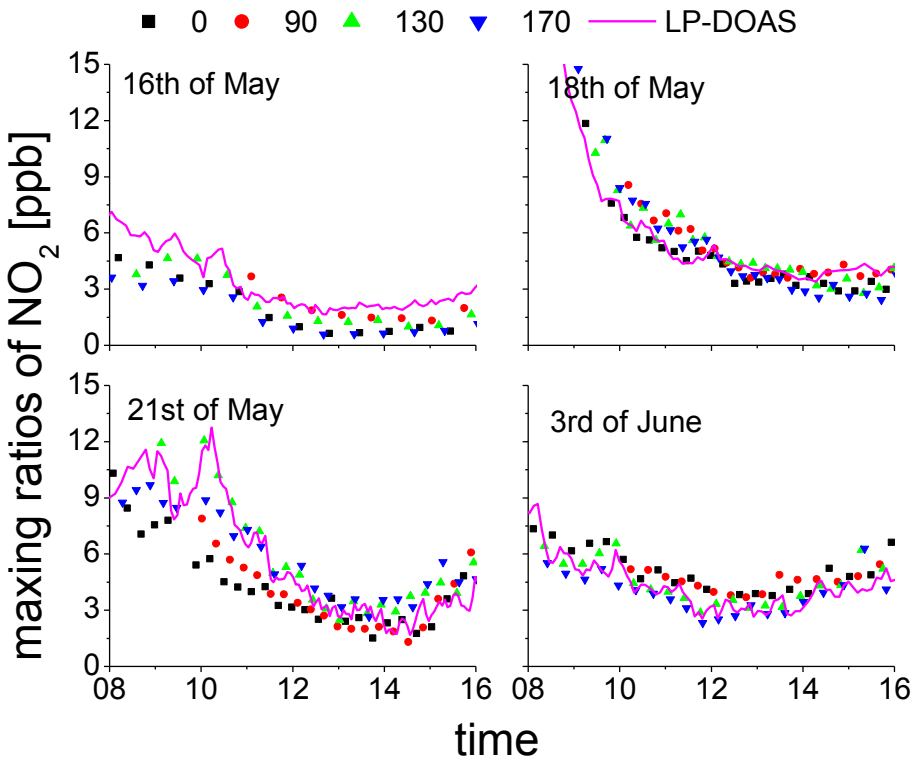


**Fig. 18.** Time series of the average $NO_2$ VMR near the ground from the rapid MAX-DOAS method compared with that from LP-DOAS. The legend of the dots is the same as that indicated in Fig. 13. The magenta lines indicate the curves of $NO_2$ VMR from LP-DOAS.





AMTD
6, 8129–8186, 2013



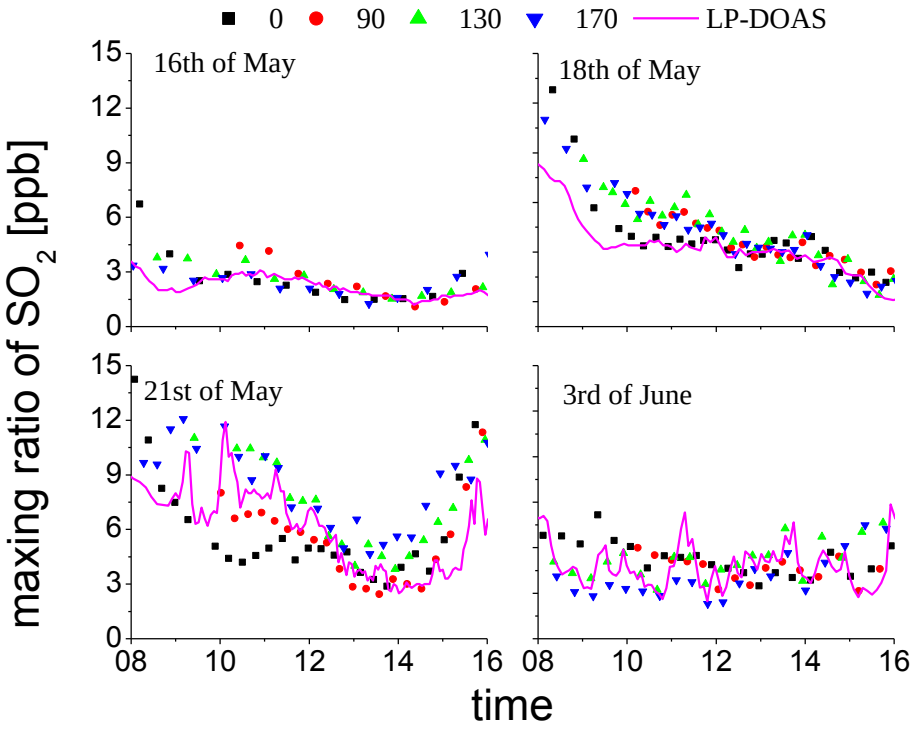


**Fig. 19.** Time series of average $SO_2$ VMR near the ground from the rapid MAX-DOAS method compared with that from LP-DOAS.





AMTD
6, 8129–8186, 2013



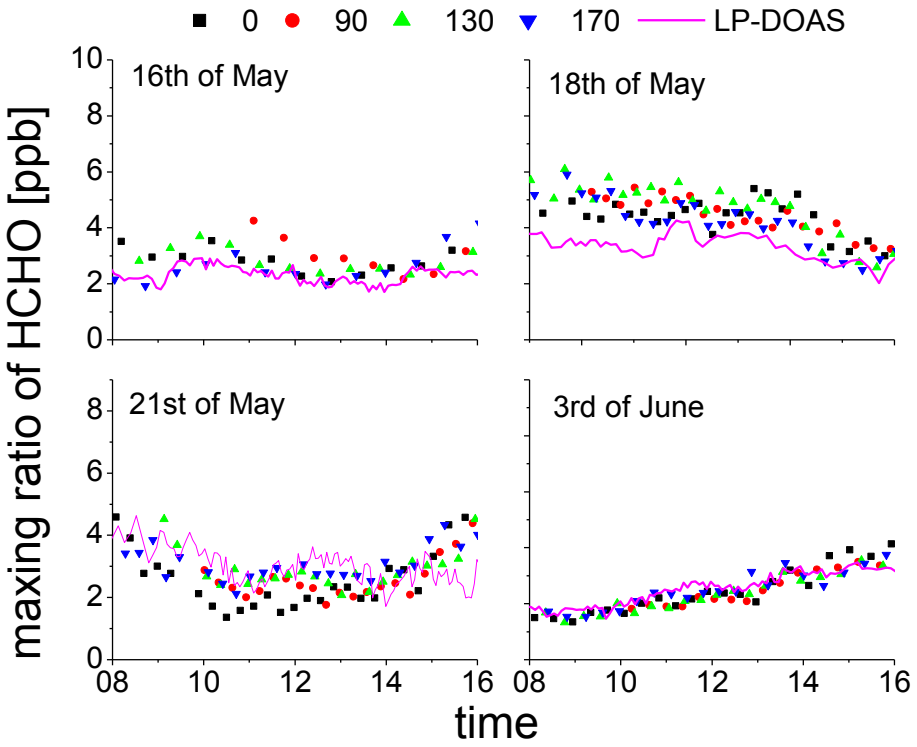


**Fig. 20.** Time series of average HCHO VMR near the ground from the rapid MAX-DOAS method compared with that from LP-DOAS.





AMTD
6, 8129–8186, 2013



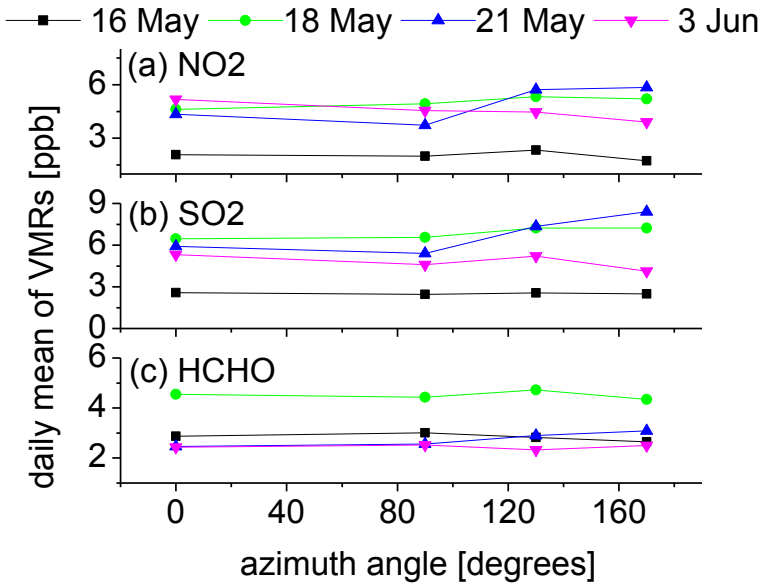


**Fig. 21.** Comparisons of the daily mean $NO_2$ **(a)**, HCHO **(b)** and $SO_2$ **(c)** VMRs near the ground for different AAs.





AMTD
6, 8129–8186, 2013



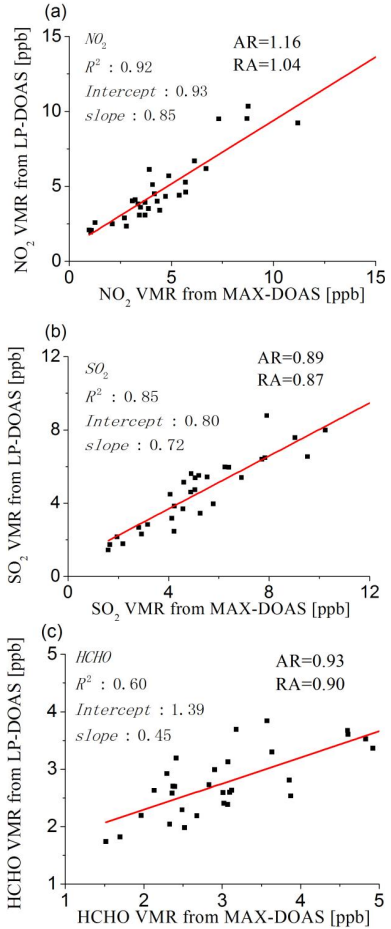


**Fig. 22.** Scatter plots and linear regression curves for the hourly average $NO_2$ **(a)**, $SO_2$ **(b)**, and HCHO **(c)** VMRs from LP-DOAS against that from MAX-DOAS.





AMTD
6, 8129–8186, 2013



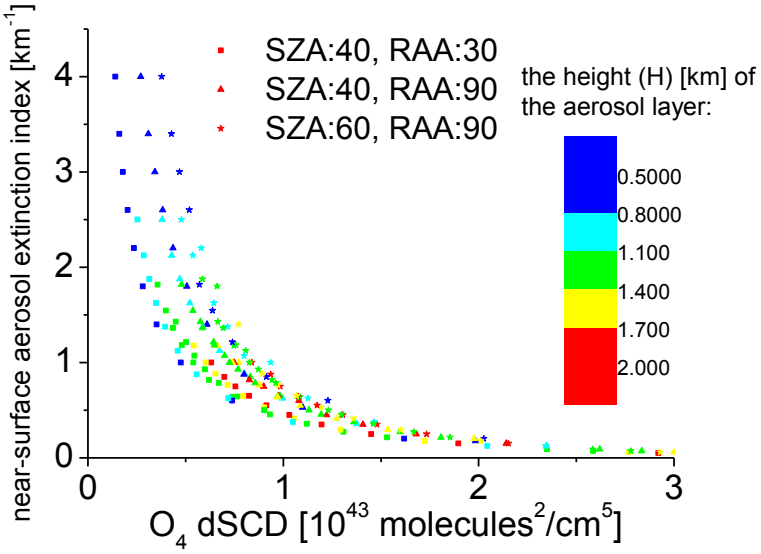


**Fig. 23.** Near-surface aerosol extinction as function of the $O_4$ dSCD measured at 1° elevation for three selected viewing geometries: Rectangles, triangles, and stars indicate simulation results for SZA 40° and RAA 30°, SZA 40° and RAA 90°, and SZA 60° and RAA 90°, respectively. The colors of the symbols indicate the height of the aerosol layer (in km).





AMTD
6, 8129–8186, 2013



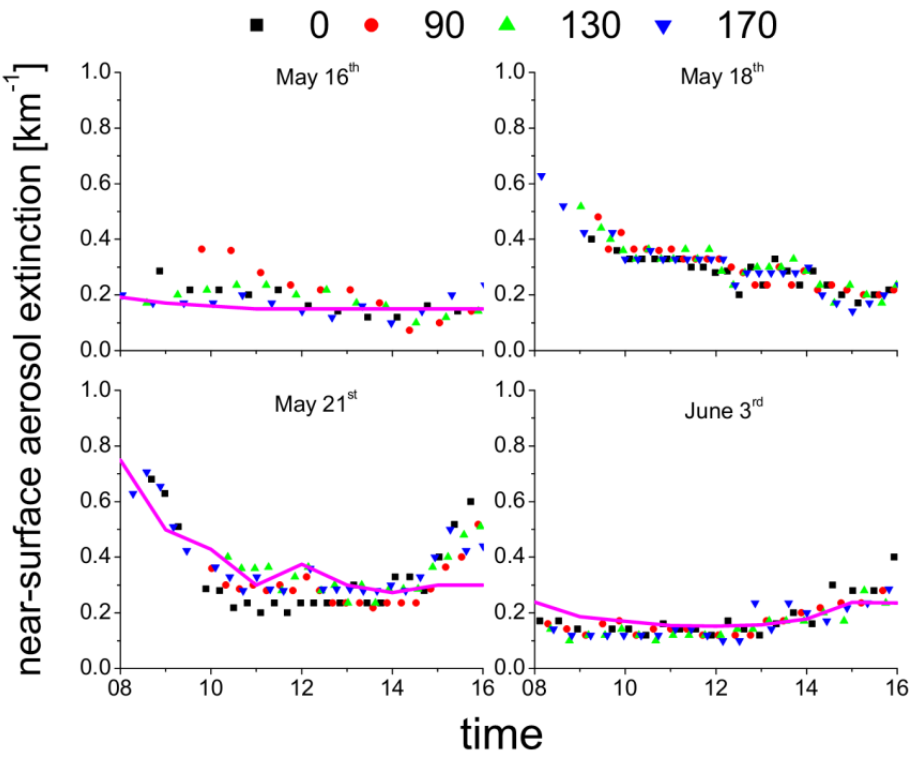


**Fig. 24.** Aerosol extinction close to the surface derived from the measured $O_4$ dSCDs for viewing azimuth angles of 0° (blue), 90° (shallow blue), 130° (green) and 170° (red), respectively. The grey lines indicate the results from visibility meter measurements at the top of the institute (16 May and 3 June) and Hefei airport (21 May) (the distance away between the experiment location and the airport site is about 20 km).





AMTD
6, 8129–8186, 2013